CALIBRATION AND TESTING OF FRET EFFICIENCY IN A VINCULIN TENSION

PROBE

By

JEREMY L STEIN

A thesis submitted to the

School of Graduate Studies

Rutgers, The State University of New Jersey

In partial fulfillment of the requirements

For the degree of

Master of Science

Graduate Program in Biomedical Engineering

Written under the direction of

Nada N. Boustany

And approved by

_____

_____

_____

New Brunswick, New Jersey

May 2019

ABSTRACT OF THE THESIS

Calibration and Testing of FRET Efficiency in a Vinculin Tension Probe

By Jeremy L Stein

Thesis Director:

Dr. Nada N. Boustany

As interest grows in the analysis of cellular level mechanical forces, including cell adhesion, cellular extension, and other microscopic-level physical phenomena, our goal is to use a previously developed Vinculin tension probe, VinTS, in conjunction with Fluorescence Resonance Energy Transfer (FRET) microscopy to quantify the mechanical forces that arise in growth cones during neuronal development. The VinTS tension probe consists of a donor and an acceptor fluorophore connected by an elastic linker inserted between the head and tail of vinculin. The work presented here aims to establish a protocol to properly correct, calibrate and convert the imaging data to FRET efficiency which is instrument-independent, and reports on nanometric changes in the distance between the donor and acceptor. For this calibration, we used control FRET constructs, with known FRET efficiency that we expressed in immortalized baby mouse kidney (iBMK) cells, bovine aortic endothelial cells (BAEC), and isolated cortical neurons. The calibration constructs consisted of either our donor, mTFP1, our acceptor, mVenus, or both connected by a long or short linker. The long linker protein was TRAF (TNF receptor associated factor) while the short linker was the amino acid sequence (GGSGGS)$_2$. These constructs were transfected into the selected cell types using Lipofectamine® LTX according to well-established protocols. All of the constructs were tested in the aforementioned cell lines. The methods involved imaging using a 3-channel

"sensitized emission" FRET methodology, with the results analyzed in a lab-developed MATLAB Script. The collected images were also corrected for background. The calibrated system was then utilized to measure the FRET efficiency in the VinTS tension probe and comparing its efficiency to that of the unloaded tension module (TSMod). The efficiency of VinTS and TSMod was measured in iBMK cells and neurons. We investigated segmentation methods to isolate the focal adhesions so that the FRET efficiency could be measured in solely those areas. So far, the investigation has allowed for calibration within the BAEC and iBMK cells, with positive results matching published FRET efficiency values for the calibration constructs. The VinTS and TSMod constructs also appear to produce expected values within the target range in iBMK cells. Current data from neuronal cells appear to have significantly more variability than the other cells which have an epithelial cell morphology. Additional data acquisition and analysis in neuronal cells is currently underway and will pave the way for further study of neuronal growth cones on substrates with various surface properties.

ACKNOWLEDGEMENTS

TABLE OF CONTENTS

LIST OF TABLES

LIST OF FIGURES

CHAPTER 1: BACKGROUND, THEORY, AND IMAGING METHODOLOGY

There has been an increase in interest in better understanding molecular level phenomena in recent years. Due to the fact that many of these phenomena occur on a nanoscale level, new techniques to study them need to be developed and optimized. This is due to the fact that conventional optical microscopy is limited by the inherent diffraction limit $\lambda/2$, where λ is the wavelength of the emitted light.[1, 2] This greatly affects subcellular imaging since many subcellular organelles and dynamic changes occur on a scale smaller than λ. [3] A variety of technology exists that enable visually observing these subcellular objects; with methods including confocal and multiphoton microscopy, 4Pi Microscopy, and Structured Illumination Microscopy (SIM). These techniques are able to achieve resolutions of approximately 100 nm, but are limited by labeling density and probe size.[3] Another methodology, which provides a spatial resolution exceeding the inherent diffraction limit and does not face the same limitations, is currently being utilized for subcellular study. [1] This technique is rooted in the work done by Theodor Förster.

In a series of papers published by Förster between 1943 and 1965, he described the foundational principles of what would become known as Förster Resonance Energy Transfer (FRET). These papers discussed energy transfer between molecules, rooted in the assumption that energy diffusion is due to energy rapidly moving between molecules, and allowed for him to derive a quantitative theory of non-radiative energy transfer. [4] In most experimental setups that have utilized this theory the molecules are usually fluorophores. Other molecules that can utilized include small organic dyes, fluorescent proteins, and quantum dots. [5] When a fluorophore is excited by light of a specific

wavelength band it emits light at another wavelength band. This happens because the photon excites an electron of the molecule into a higher energy state, that when the electron returns to its ground state, will release a photon of another lower energy and longer wavelength. This is termed a Stoke's Shift.[6] A FRET-based imaging approach, its use, and its methodology will be described in the following.

1.1: An Introduction to FRET and Its Associated Physical Properties

1.1.1: What is FRET?

Fluorescence Resonance Energy Transfer (FRET), a form of the theory derived by Förster, is a nonradiative transfer of energy from one fluorophore, termed the Donor, to another, termed the Acceptor, via a long-range dipole-dipole coupling mechanism. [7] This transfer requires that the two fluorophores are within 1-10 nm, or 10-100 Å, of one another. [8, 9] An additional requirement is an overlap of the emission band of the Donor, with the excitation band of the Acceptor. This ensures that the donor emission and acceptor excitation frequencies are the same during transfer and that the energy amount is quantized.[10] This overlap of the spetra is shown in Figure 8 later on in this Chapter.
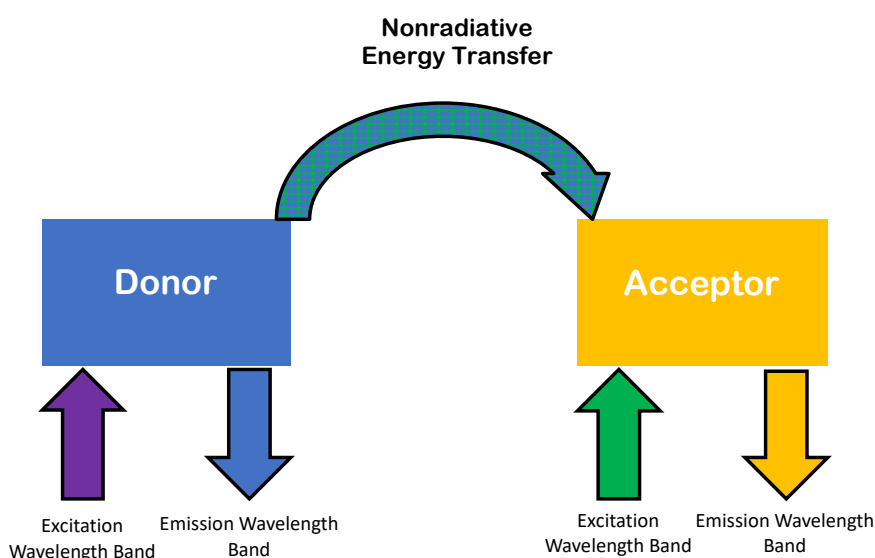
Figure 1: Overview of a FRET Pair

This energy transfer can be quantified by its efficiency, which is termed FRET

Efficiency (E_{FRET}). FRET Efficiency is inversely related to the separation distance

between the donor and acceptor. This means that the closer the fluorophores are to one

another, the higher the Efficiency. Part of Theodor Förster work included the

quantification of E_{FRET}, which is dependent on an inverse sixth power relationship to the

Förster Critical Distance (R_0) and the molecular separation distance (d). (Equation 1) R_0

is defined as the distance where the energy transfer rate is equivalent to the rate of

fluorescence emission, or a FRET efficiency of 0.5 (50%) It is calculated using the

overlap integral, the quantum yield of the acceptor, the lifetime of the donor in the

absence of an acceptor, and the effective index of refraction; all quantifiable parameters.

[4] When d equals R_0, we achieve a FRET Efficiency of 50%.

$$\text{FRET Efficiency} = \frac{(R_0{}^6)}{(R_0{}^6)+(d^6)} = \frac{1}{\left(\frac{d}{R_0}\right)^6+1}$$

Equation 1: Calculation of FRET Efficiency using R_0 and d

FRET Efficiency is also not the only way to quantify FRET, another way is

through Fluorescence Lifetime Imaging Microscopy (FLIM). There are two main type of

FLIM systems. The first is Frequency-domain FLIM, which uses a laser light to excite

the sample then measures the modulation of the fluorescent signal and phase delay

relative to the excitation light. [11] This measures the fluorescence lifetime, or the

characteristic time a molecule remains in an excited state before returning to its ground

state. This is usually defined as the time it takes for the florescent intensity to decay to

1/e, or about 37%, of the initial intensity. [12] FLIM, similar to FRET, can also be used

in the study of Protein-Protein interactions within cells and is able to localize them to specific cellular compartments. [13, 14]

The similarity of the applications of the two modalities opens up the possibility of combination, which has been done, leading to the second type of FLIM. This type of setup, which combines the two modalities, is called FLIM-FRET. FLIM-FRET Microscopy works by measuring at the lifetime of the Donor in the presence of the Acceptor and then of the Donor alone, to determine the distance between the two fluorophores. [15] FRET-FLIM is seen as advantageous because it is independent of fluorophore concentration and excitation light path. [14] These advantages may be offset by the extensive setup required for FLIM-FRET and the careful calibration required. In addition, traditional microscope-based FRET systems also afford the user more ability to modify the setup to best fit the cell type or FRET pair. [12]

The selection of fluorophores is a key part of experimental procedures. As the composition of these pairs has a dependence on a variety of factors, one of the most important being the maximization quantum yield of the donor. [7] An area that has seen much growth in recent years is the that of Fluorescent Proteins (FPs), with several FRET pairs composed of proteins utilized in the field. FPs can be constructed more easily, have a high cellular specificity, and can be readily introduced to cells in vitro and in vivo. This is contrasted to organic dyes and quantum dots, which are not stable in the body and quickly cleared.[5] It is also necessary for the two fluorophores to have the same maturation, meaning that they are produced at the same rate. This is necessary to maintain a theoretical ratio of 1, meaning that there is an acceptor for each donor, which is important in certain methodologies, including the one described here. [5] Due to these

extensive requirements, it can be difficult to find optimal FRET pairs, so once one is found it is frequently utilized.

Several of the most common FP FRET pairs are composed of derivatives of Teal Fluorescent Protein (TFP) and Yellow Fluorescent Protein (YFP), both of which are derived from Green Fluorescent Protein (GFP). [5] They are an optimal pair due to the fact that the emission band of TFP overlaps with the excitation band of YFP, as well as the good quantum yield of TFP. The fact that they are both GFP-derived means that they have similar maturation rates, further bolstering their use as a pair. One of these derivative pairs is monomeric TFP (mTFP1) and mVenus, both have been shown to be one the best variations of TFP and YFP, respectively.[16] The mTFP1 fluorophore has excitation and emission wavelength bands centered at 462 nm and 492 nm respectively. [5, 17] The mVenus fluorophore has excitation and emission wavelengths centered at 515 nm and 528 nm respectively. [5, 18-20]

There are several key aspects that one must understand to understand FRET. One of the most important is the separation of the fluorophores. As mentioned in the chapter introduction, the two fluorophores must be within a specific range for FRET to occur. If the separation distance exceeds this range, FRET will not occur, and no energy transfer will be measured. In addition, the E_{FRET} is directly related to the separation of the fluorophores, as the farther apart the they are the lower the efficiency of energy transfer. This has several applications which will be discussed in the next section. Another necessary consideration is an overlap of their excitation and emission bands. As previously mentioned, this ensures that the energy being transferred is quantized. If this overlap is not present, there will be no interaction of the fluorophores, and FRET will not

occur. The contrast of the obtained images of the sample is similar to those of conventional fluorescence, where it is a comparison of the fluorescing cell and the background, where no fluorescence should be present.

1.1.2: The Uses of FRET

FRET has many uses in a variety of research disciplines. These areas include Protein-Protein Interactions, Protein-DNA Interactions, Protein Conformation Studies, Gene location, and the measurement of forces on the subcellular level. Each of these areas utilize FRET in a different way, since each have a specific end goal. Within the area of Protein Conformational Studies, FRET is of great use as it allows for domain distances to quantified. This is possible because E_{FRET} is directly related to the separation distance of the fluorophores. A very potent example is the modification of the behavior of proteins, such as kinases and small GTPases, in cancer cells, which makes FRET optimal for the study of anticancer drugs.[21] FRET can also be used as a binary marker to indicate the presence of injury within cells. This is done by using the two FRET fluorophores to mark two proteins, Bcl-2-associated death promoter (BAD) and B-cell lymphoma-extra-large (Bcl-xL), which usually remain more than 100 A apart. Upon injury the BAD enters the mitochondria and suppresses the Bcl-xL, bringing the two molecules within range, producing a FRET signal. [15, 22] In a similar fashion, microscale, subcellular distances and forces using FRET in vitro and in vivo can be studied.

In vivo imaging, while plausible, is not without its drawbacks. One of the most important of them is the toxicity of the probe. This is particularly true with the use of Quantum Dots; whose toxicity increases with concentration.[23] The in vivo applications

would include gene localization and cellular structure identification. It could also allow

for membrane function monitoring and the study of macromolecule interaction within

organisms.[9] Another hinderance though is the shallow penetration of visible light,

limiting current trials to small volume areas. Some studies using Near-Infrared (NIR)

light, along with constructs tuned for these wavelengths, but the penetration depth issue is

still present.[24] These complications make further development and testing necessary, as

many current applications are dependent on the development of constructs. These

constructs need to be tuned for their application, have a reduced toxicity, and be able to

be visualized. This means that many applications in vivo are limited to superficial areas

where excitation light can reach the area of interest. These obstacles have inhibited

widespread in vivo testing, so in vitro uses are the main use for FRET.

The in vitro testing done utilizes cultured cells, which are then transfected with

the FRET construct encoded on a plasmid. This method of study allows for analysis of

cellular behaviors and interactions. The area of focus for the experiments described in

this thesis is the measurement of forces within cells, as they are not completely

understood.[25] There are several FRET-based tension sensors that have been utilized to

better understand these intracellular forces, some targeting the vinculin and actin

proteins.

1.2: An Overview of the FRET Probes Used

The probe utilized in these studies, VinTS, is optimized to insert itself into the

vinculin protein after amino acid 883, between areas termed the "vinculin head" and

"vinculin tail" domains. [26] When the construct, which is encoded onto a plasmid, is

transfected into the cell, the construct is produced as a part of the vinculin protein. The

VinTS probe itself is composed of a specialized TSMod construct, consisting of the two aforementioned fluorophores connected by (GPGGA)$_8$, a 40 amino acid long elastic linker. [25] This linker being elastic is key in allowing for force measurements. Since the proteins can be pulled further apart from one another when the protein is experiencing a tensile force. This distance is the basis of the force measurement derived from the probe, as it allows for us to conclude that the separation of the fluorophores aligns with the forces on the protein. This is possible since the probe was previously calibrated to determine how much EFRET corresponds to the forces on the elastic linker. Since we can obtain measurements in terms of EFRET, the results can be compared between samples and cell types. A schematic of the probe inserted into a vinculin protein is shown in Figure 2. Previous studies have shown that this probe can measure forces up to approximately 8 pN, but the exact range of sensitivity is still being determined.[25, 27] The VinTS construct used was supplied by Addgene.

Figure 2: Schematic of the VinTS FRET Construct

In addition to our measurement construct, VinTS, we utilized a series of control constructs for calibration. This included a Donor Only construct, Acceptor Only construct, a long linker construct, a short linker construct, and TSMod. The Donor Only and Acceptor Only constructs were plasmids that encoded just the mTFP1 or mVenus protein individually. The linker constructs were plasmids that encoded for the two fluorophores and with a linker between them. The long linker that was utilized was TNF-associated factor (TRAF), shown in Figure 3. [28] The short linker was the amino acid

chain (GGSGGS)$_n$ where n is a variable number of the constructs, which allows for it to be made shorter than the TRAF linker. In this case, the linker was composed of two chains, so n was equal to 2.[29] This probe is shown in Figure 4. Both of the plasmids that encode these control probes we obtained from the lab of Dr. Brent Hoffman. The TSMod construct is composed of the two discussed fluorophores, mTFP1 and mVenus, connected by an elastic linker that is 40 amino acids long, and has an expected E$_{FRET}$ of about 0.286.[25, 29] This known E$_{FRET}$ allowed for further study and calibration of the system, by providing a known basis for comparison. This construct was obtained from Addgene and is shown in Figure 5.
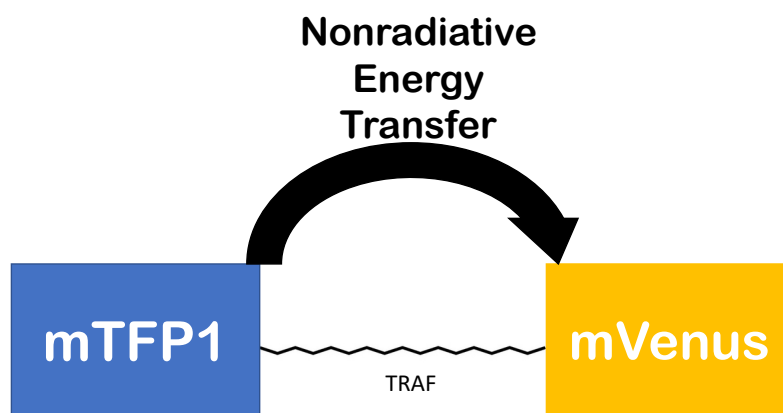
Figure 3: Schematic of the TRAF Long-Linker FRET Construct
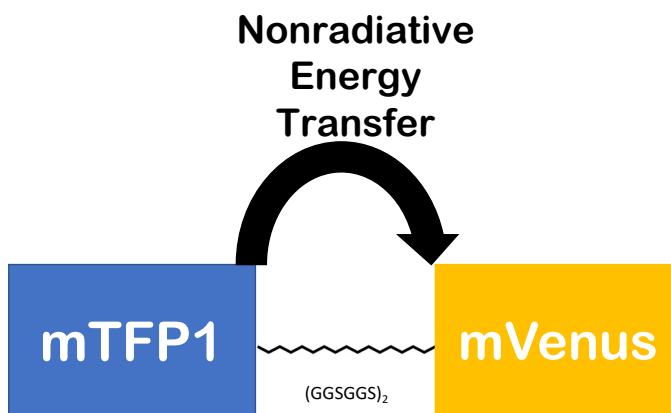
Figure 4: Schematic of the (GGSGGS)$_2$ Short-Linker FRET Construct
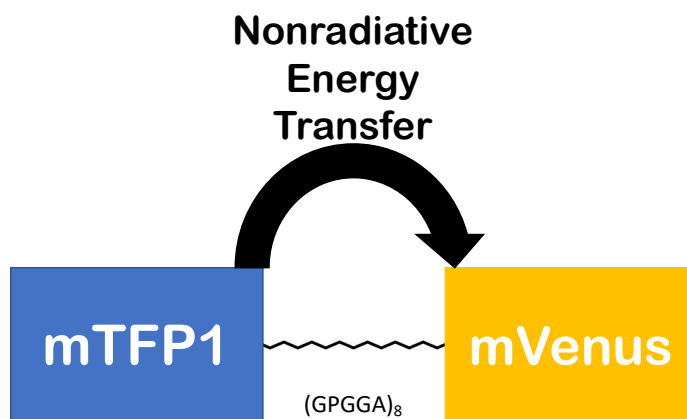
Figure 5: Schematic of the TSMod FRET Construct

1.3: An Overview of the Tested Methodology and the Technology Required

The methodology of our experiments began with the insertion of a series of FRET

constructs into a variety of cell types and obtaining images of the cells using a computer-

controlled microscope. This setup uses a Hg Arc-Lamp and a series of filters to excite

and measure the sample. The lamp produces a very broad-band light beam, which is

adjusted using the filters to produce a very narrow band around the Excitation

Wavelength Band of the Donor or Acceptor. Another set of bandpass filters are used to

measure the fluorescence emission of the sample. These filters will correspond to with

the Emission Wavelength Band of either the Donor or Acceptor fluorophore. Because the

use of these filters needs to occur very quickly, it is necessary to automate the

process.[29] If the filters are not switched fast enough, a time delay between the images

is introduced. This adds additional complications to the processing methodology, that are

better off avoided. A halogen light source was also used for bright field view and

focusing of the sample. A filter was also used to limit photobleaching during focusing.

The computer used an image acquisition software to obtain data from this setup and

saved them for later analysis. [26] These images were then processed in a MATLAB

code created for this purpose. The results from this code are then analyzed quantitatively and qualitatively, with each approach designated for a specific purpose.

Our setup was based around a Zeiss Axiovert 200m microscope with 40x and 63x objectives. The 63x objective was the objective utilized for most of the studies, with the 40x used for introductory testing early in the process. Images were obtained through the use of a dichroic mirror filter cube (T450/514rpc; Chroma Technology Corp.) and a series of Excitation and Emission Filters. The filters consisted of a mTFP1 excitation filter (ET450/30x; Chroma Technology Corp.), mTFP1 emission filter (ET485/20m; Chroma Technology Corp.), mVenus excitation filter (ET514/10x; Chroma Technology Corp), and mVenus emission filter (FF01-571/72; Semrock). This set of filters have been used as set in previous experiments with the probe, with positive results. [30, 31] The spectra of each of the filters, obtained experimentally and retrieved from the Semrock Searchlight spectra viewer, are shown in Figure 6. [16, 20] Images were obtained using the IPLab Image Acquisition Software and saved for processing. A schematic of the setup can be seen in Figure 7.
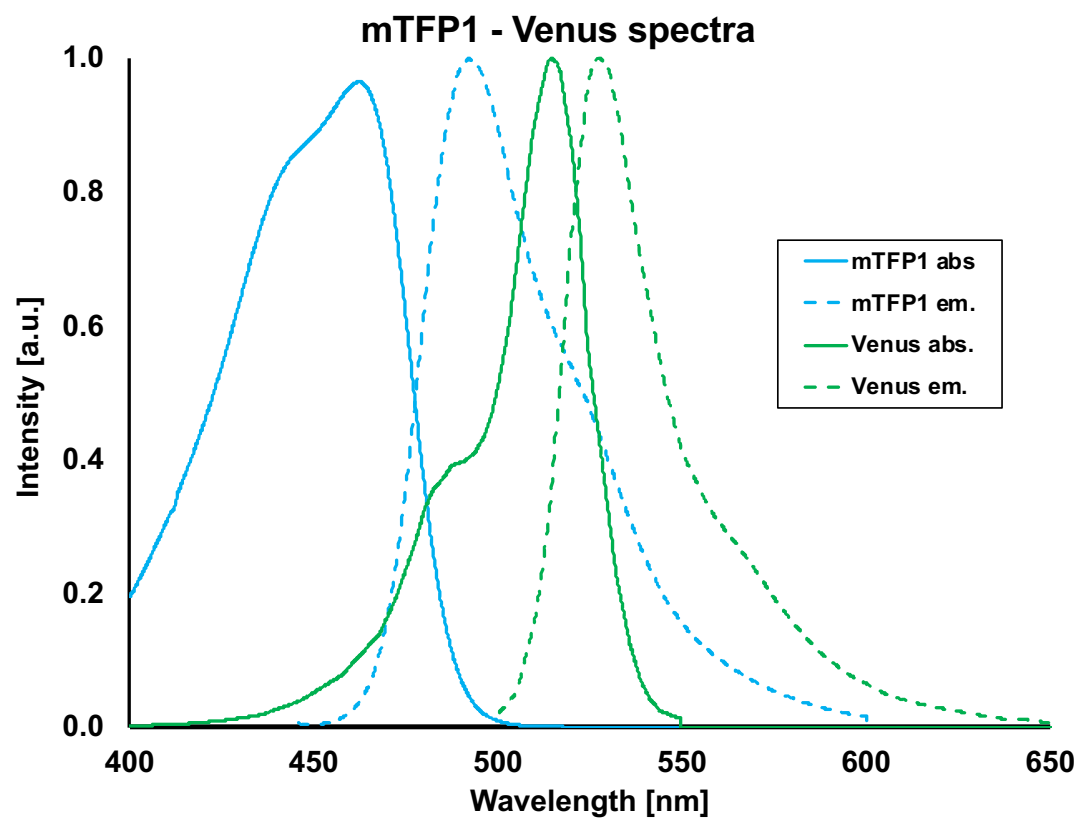
Figure 6: Spectra of the Filters Used
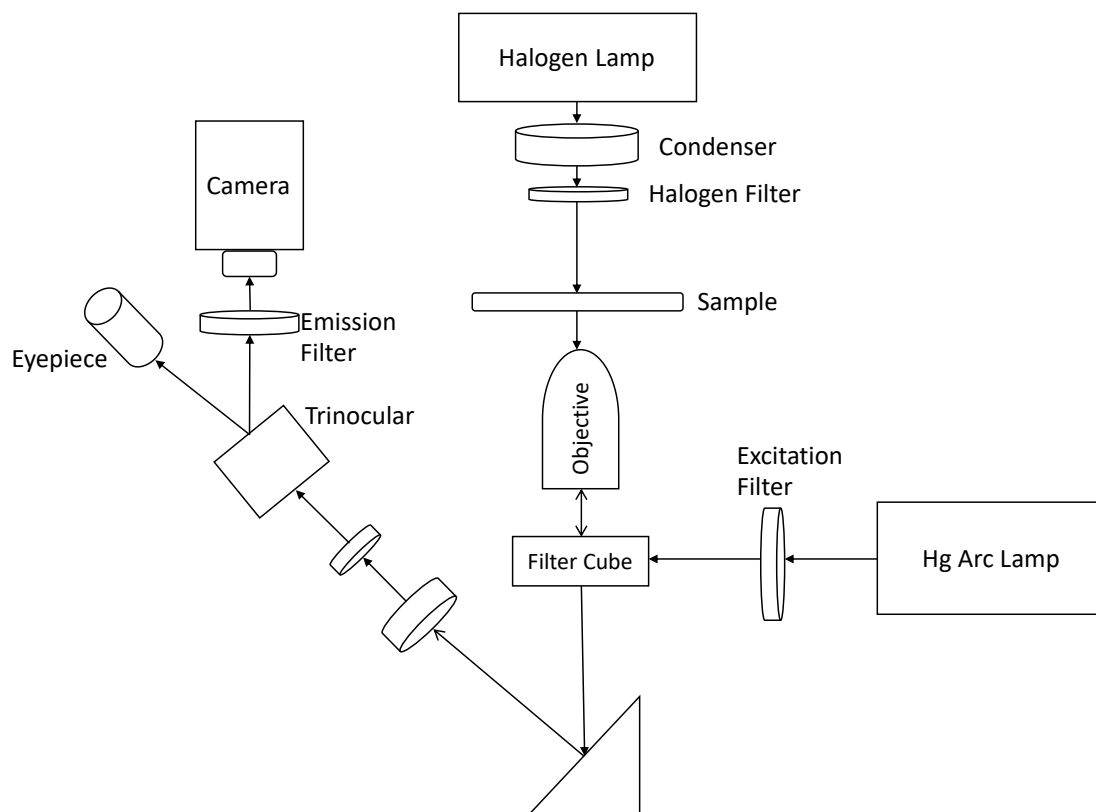
Figure 7: Schematic of the Imaging Setup

The cell lines were cultured in a 12-well plate, with wells of area of 4 cm^2. Within the wells, removable glass coverslips were placed on which the cells were able to grow. These coverslips are cleaned before they are placed into the culture plate, by soaking the coverslips overnight in Chromic Sulfuric Acid. They are then washed with Distilled Water and rinsed in Methanol. After rinsing, they are left to dry in a Biosafety hood before they are plated in the multi-well culture plate.

These removable glass coverslips are used so that they cells can be removed from the plate for imaging. These coverslips are mounted on a custom metal plate that has machined specifically for this purpose. On one side of the metal plate a large square coverslip is sealed to the plate using vacuum grease. On the other side a layer of vacuum grease is applied, then the cell-coated coverslip is placed on the metal plate. The

coverslip is then sealed using Valap Sealant.[32, 33] The plate is then filled with imaging medium before it is mounted onto the microscope for image acquisition.

1.3.1: Imaging Methodology: 3-Channel Sensitized Emission

One of the methods to study FRET is 3-channel Sensitized Emission, which involves obtaining 3 images then the use of several published formulas to calculate FRET Efficiency. [8] FRET Efficiency is used since it is situationally independent. This means that results reported this way can be reproduced in an entirely different system, possibly in a different way. Each of these images are taken after stimulation at a specific excitation wavelength band and measured through a filter to isolate specific emission wavelength band. This is important as each image serves to aid in the overall calculation of FRET Efficiency within the cell.

These 3 images can be obtained simultaneously or in very quick succession. [8, 29, 34, 35] This aims to minimize changes in the cell between the taking of images and is why the aforementioned filters need to be changed quickly. In these experiments, the 3 images were taken in quick succession with very short exposure times. This is important as to minimize the possibility of photobleaching from excessive exposure. It was found that the variability of exposure time and intensity plays a major role in the calibration of the system, so proper understanding and testing is needed to optimize the procedure.

The first image that is taken is called the FRET Channel. This image is also called the DA image, because it is obtained with stimulation at the Donor Excitation Wavelength Band but measured at the Acceptor Emission Wavelength Band. This image should allow for measurement of FRET directly from the sample, as the only signal visible should consist of the energy transferred from the Donor to the Acceptor. This is

due to the fact that any Donor emission should not be visible in this image, and that the Acceptor is not being excited directly at its excitation wavelength band. While, in theory, this seems straightforward, in practice, a major complication is encountered.

A phenomenon known as bleedthrough occurs when imaging samples using a 3-Channel Sensitized Emission methodology. Bleedthrough exists in two forms, Acceptor Bleedthrough and Donor Bleedthrough. Acceptor Bleedthrough is occurs when the Acceptor molecule is excited by the Donor excitation wavelength band. Donor bleedthrough occurs when the Donor molecule emits at the Acceptor emission wavelength band. To properly correct for Bleedthrough in a 3-channel Sensitized Emission methodology, two images are obtained; the DD and AA images. The DD image is excited at the Donor excitation wavelength band and measured at the Donor emission band. The AA image is obtained in a similar fashion, but at the Acceptor wavelength bands. Each of these images allows for us to understand the fluorescence measured in the presence of just one of our molecules, as we are measuring solely at either the Donor or Acceptor Excitation and Emission Wavelength Bands. The obtained images were named DD, for the case of Donor Excitation and Emission, and AA, in the case of Acceptor Excitation and Emission. The DD image is the quenched fluorescence of the donor, meaning that the emission of the Donor molecule observed is not the full emission, but the remaining energy that is not taken up by the Acceptor. The AA image would therefore also contain more signal that what the Acceptor would emit alone, as it has taken up additional energy from the Donor. An updated spectra diagram of the probes is shown in Figure 8, with the bleedthrough areas and necessary spectra overlap shaded.
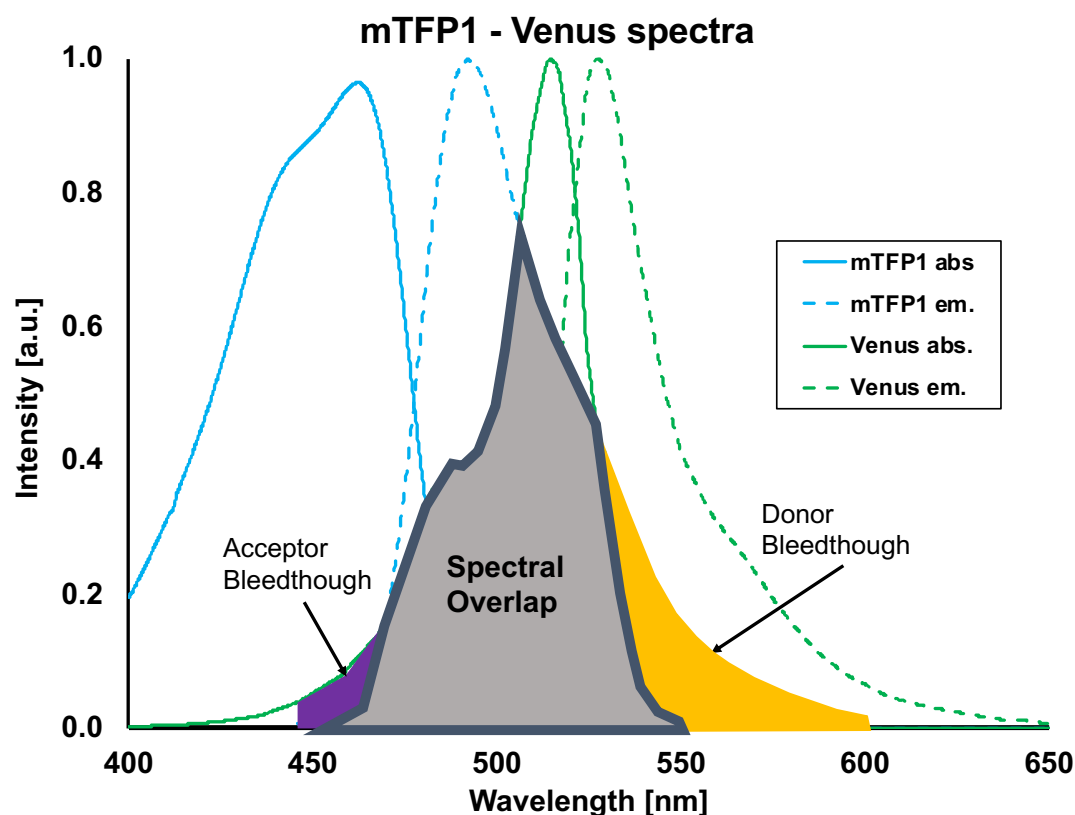
Figure 8: Spectra of the Filters showing the location of Acceptor Bleedthrough, Donor Bleedthrough, and the Spectral Overlap

Another issue that could arise is that of Cross-Talk. This is when a fluorophore causes a signal in the opposite channel, such as the donor causing a signal in the AA image. [26, 36] This issue is corrected by the setup itself. To determine that Cross-Talk was minimized, images of the Donor Only and Acceptor Only constructs were analyzed. The DD/AA ratio in the Acceptor Only images and the AA/DD ratio in the Donor Only images was measured. Since in both cases the values were close to zero, it can be concluded that Cross-Talk has no effect on the measured signal.
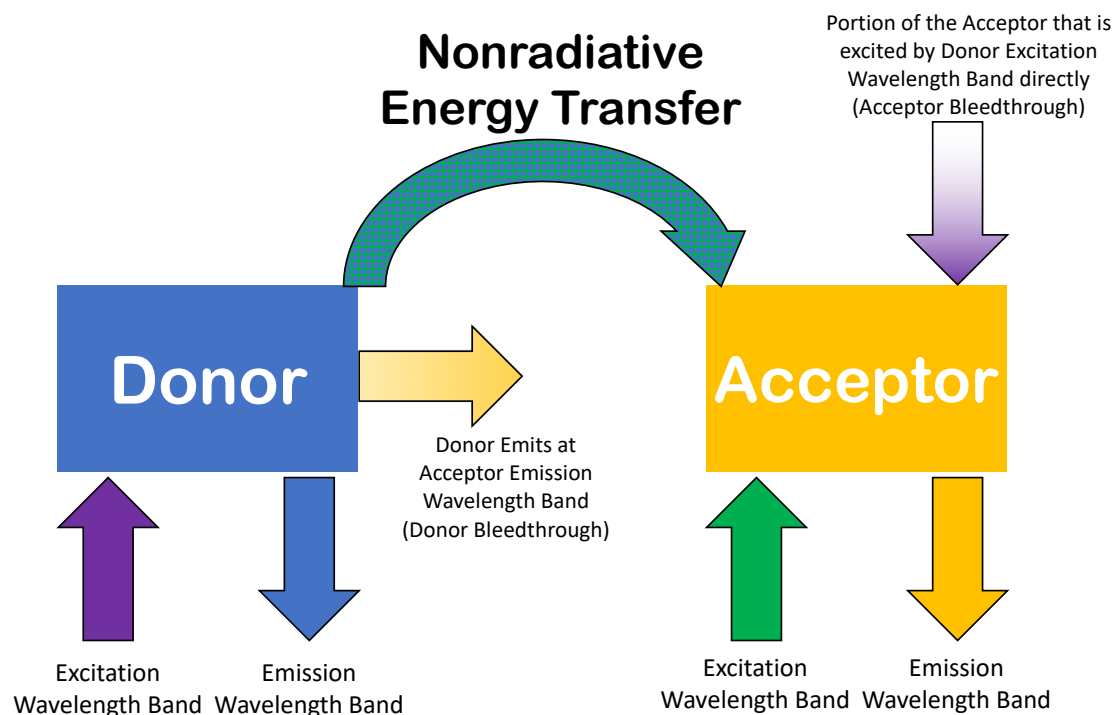
Figure 9: A FRET Pair imaged with 3-Channel Sensitized Emission

There is also the possibility of cellular autofluorescence. This is the signal that is measured due to endogenous fluorophores within the cells. This complicates the computational cellular isolation process, as the true background becomes harder to calculate. The true nature of how much signal is given off by cells that are not expressing the FRET construct is what is the issue here. This problem is one that must be thoroughly investigated to properly be corrected for. As will be discussed in the next section, multiple approaches were tested to determine the optimal method for correction.

1.3.2: Analysis of Data using a lab-developed MATLAB Code

We utilized a code developed in the MATLAB environment to analyze our obtained images. This allowed for automation and image-wide calculations to be done. This is important as all formulas developed to calculate FRET Efficiency must be done on a pixel-by-pixel basis. This is important as it allows for the integrity of the image to be

maintained, so that each step of the process can be visualized as it is completed. It is important to also note that the computation processing done in MATLAB was optimized for each of the tested cell type classifications based on cell shape.

Before any operations can be performed on the images, a background correction method must be applied. This method must account for the possibility of autofluorescence of non-expressing cells within the image. Since the fluorescent cells were sparse in the sample, the approach devised and utilized is a pixel histogram method, where the values of all pixels in the image are sorted in 713 bins. The value of the bin with the largest count of pixels is determined to be the background and the max value of that bin is used to threshold the image. The theory behind this approach is that there is a standard autofluorescence in the area of interest and that by using the maximum value of the bin, a slight overcorrection is being applied. In addition, a camera offset could be applied to all pixels in the image. This is a standard value that is inherent to the camera being utilized to acquire the image. In our trials and processing, a value of 105 would subtracted from all pixels. This value, however, is not subtracted from the image, as the histogram method inherently includes this offset.

The first step in the process is the calculation of the Donor and Acceptor bleedthrough(s) for our instrument. As mentioned before, images were obtained at Donor Excitation and Emission Wavelength Bands, as well as Acceptor Excitation and Emission Wavelength Bands for samples consisting of cells transfected with the donor only, or with the acceptor only fluorophore. Each of these images were used to calculate their respective Bleedthrough. To calculate the Bleedthrough, we use a linear regression method. We make a scatter plot of the pixel values of the DA image and plot it against

the respective fluorophore channel. This means that for Donor Bleedthrough, we plotted the DA image against the DD image. A linear fit was then calculated, with the slope of this line being the Bleedthrough value. This works to give the Bleedthrough as, in the case of 100% Bleedthrough, a line with a slope of 1 would be calculated, as each pixel from each image would be exactly the same. This line therefore gives the ratio of each pixel to its corresponding pixel between the two images, allowing for the determination of how much of one image is present in the other; the Bleedthrough for that fluorophore. The same process was done to calculate Acceptor Bleedthrough; where the DA image was plotted against the AA image. An example of a Donor Bleedthrough calculation is shown in Figure 10.
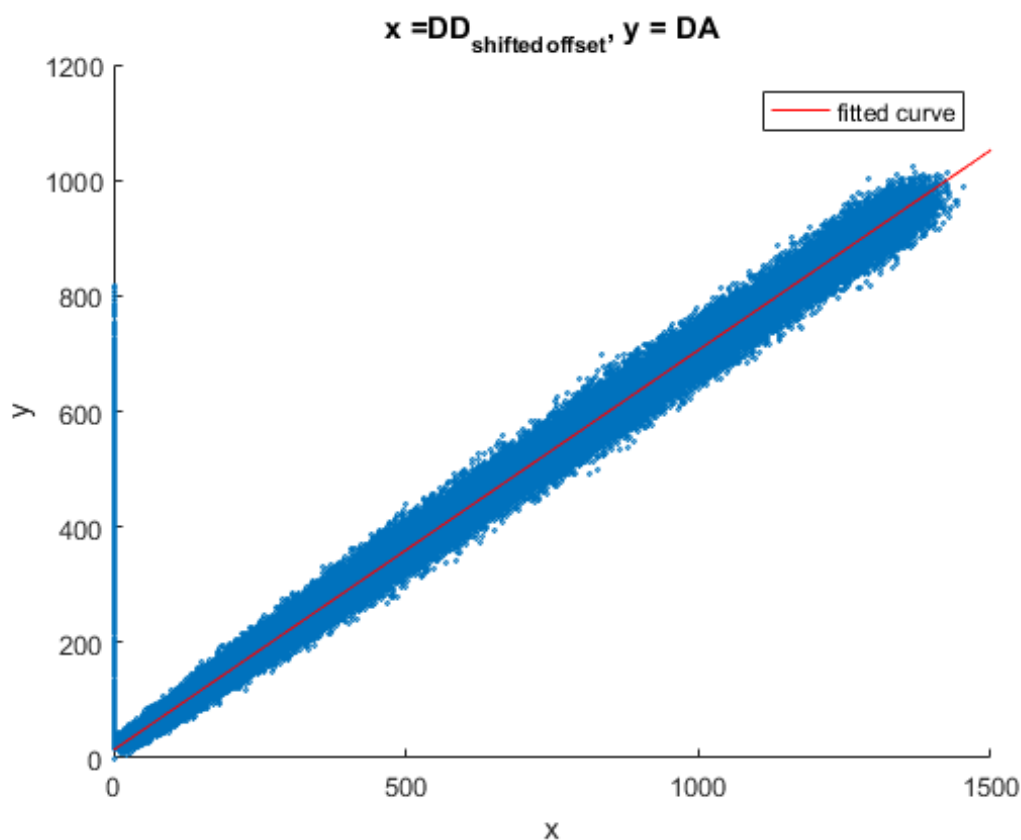
Figure 10: Donor Bleedthrough Example of a Linear Regression Scatter Plot

Once the Bleedthrough values are calculated we can apply a correction to the measurement in the FRET channel for a sample containing the FRET construct with both the donor and acceptor present. This is done via a reduction method, where the DD and AA image are each multiplied by their respective Bleedthrough value then subtracted from the DA image, as demonstrated in Figure 11. The image calculated from this is called the FRET Corrected, or F_c image.[8]
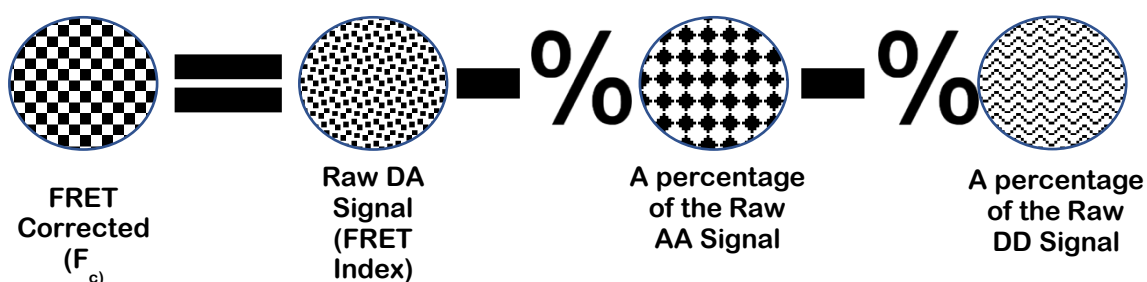
Figure 11: Calculation of Corrected FRET Image

This newly calculated F_c image, along with the obtained AA and DD images are used to calculate the G Factor. This G Factor allows for us to relate an increase in sensitized acceptor emission to a loss in donor fluorescence. [37] We need to make this type of correction due to the fact the F_c alone may be instrument dependent which makes results from different setups not directly comparable. [8] This G Factor requires two FRET constructs containing our Donor and Acceptor fluorophores connected by a linker, one long and one short. These were the aforementioned GGS and TRAF constructs described in Section 1.2. The G Factor calculation formulation is shown in Equation 2.

$$G\ Factor = \frac{\left(\frac{Fc}{AA}\right)GGS - \left(\frac{Fc}{AA}\right)TRAF}{\left(\frac{DD}{AA}\right)TRAF - \left(\frac{DD}{AA}\right)GGS}$$

Equation 2: G Factor Calculation

To obtain the F_c/AA and DD/AA images, a linear regression method, similar to that used for Bleedthrough calculations, is used. In each case, the two images are plotted against one another on a pixel-by-pixel level to create a scatter plot. Once this plot is created, a linear fit is calculated. The slope of this fit is the value that is recorded for that variable. These values are the average F_c/AA and DD/AA values for that image set. After calculation, the values are stored in a table for use in Equation 2 and Equation 3.

Once the G Factor has been calculated, the FRET efficiency, E_{FRET}, can be mathematically quantified. This is done using Equation 3. This formulation can be used for all samples from a particular setup, as the G Factor is a constant for a specific FRET pair and imaging setup. [8] As all the aforementioned calculations are done on pixel level, proper processing must be done before values are extracted from the code. These include the aforementioned image shifts and background subtraction. [29] If these procedures are not done, it can greatly affect the calculation of the G Factor and thereby the E_{FRET}.

$$E_{FRET} = \frac{\left(\frac{Fc}{AA}\right) * \left(\frac{1}{G}\right)}{\left(\frac{DD}{AA}\right) + \left(\left(\frac{Fc}{AA}\right) * \left(\frac{1}{G}\right)\right)}$$

Equation 3: FRET Efficiency Calculation using G Factor with Corrected FRET Index,
Donor Channel Image and Acceptor Channel Image

CHAPTER 2: CALIBRATION AND MEASUREMENT IN CONTROL CELL LINES

As discussed in Chapter 1, the VinTS probe is designed to insert itself into the Vinculin protein. Vinculin is found in an area of cells called Focal Adhesions. Focal Adhesions are "complex intracellular linkages between integrins and the F-actin cytoskeleton that both transmit and respond to mechanical forces."[25] They act as anchoring sites for cells in culture and play a key role in cellular locomotion. The focal Adhesion sites act to convert mechanical signals to chemical ones, a process known as mechanotransduction. [38] Since these areas experience a quantifiable mechanical force, they are an ideal candidate for study.

Focal Adhesions arise in a variety of cell types in culture. The two control types that were studied and will be discussed were immortalized Baby Mouse Kidney Epithelial (iBMK) and Bovine Aortic Endothelial Cells (BAEC) lines. An important consideration when comparing the cell types is the Days-In-Vitro (DIV) of the culture. The iBMK cell line is an easy to culture line that will not age, as it has been modified to become an immortal cell line, that is also known to be able to be transfected and produce a readable signal. This meant that the culture only needs to be split when it became too confluent. The BAEC line does age but is known to transfect well and produce a stronger signal than the iBMK line. Both lines were tested to demonstrate consistency and a range of applicability of our system.

2.1: Cell Preparation and Transfection

The cell platting, and plasmid insertion methodology was the same for both cell lines. Each cell line was platted in a 12-well plate at a density of 10,000/cm². Each well contained a glass coverslip, that was cleaned in chromic sulfuric acid beforehand. This

soaking sanitizes the coverslips to ensure that there are no possible sources of contamination. No coverslip coating is necessary, as both cell lines are able to grow directly on glass. Once the cells were plated into the wells, the cells were left in culture to grow for 1-2 days. This allowed for them to become 70-90% confluent, a necessary aspect of our transfection protocol.

Both of the cell lines were transfected using a Lipofectamine® LTX protocol. This is procedure uses two reagents, Lipofectamine® LTX and PLUS™ Reagent, developed by Thermo-Fisher Scientific to insert a DNA plasmid into our tested cell lines without the use of a viral vector. The procedure for preparation of this solution is shown in Figure 12.
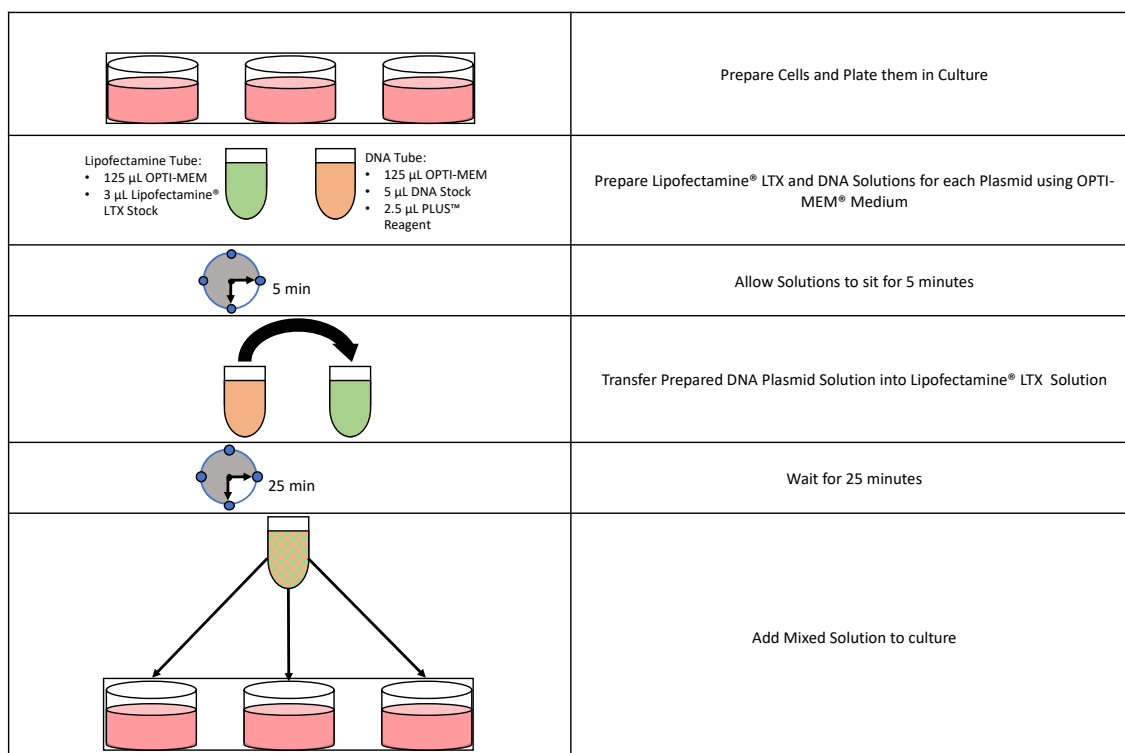
Figure 12: Overview of iBMK and BAEC Lipofectamine® LTX Transfection Procedure

An important note is that the culture medium that the cells are growing in must be aspirated and replaced with antibiotic Free Culture Medium or OPTI-MEM® Medium before the addition of the Lipofectamine® LTX-DNA mixture. The culture, after the addition of the mixture, is then placed in the incubator for 3 hours. This allows for the plasmids to be inserted into the cells. After the incubation period the medium, whether PEN/STREP Free Culture Medium or OPTI-MEM® Medium, is then aspirated and replaced with PEN/STREP Medium. It is then placed back into the incubator allow time for the cells to begin to properly express the transfected plasmid and the fluorescence to become visible.

```
┌─────────────────────────────────────────┐
│            Load Raw Images               │
└─────────────────────────────────────────┘
┌─────────────────────────────────────────┐
│  Dilation of Images using Disk sizes of  │
│           15 and 256 (VinTS Only)        │
└─────────────────────────────────────────┘
┌─────────────────────────────────────────┐
│              DD Shift                    │
└─────────────────────────────────────────┘
┌─────────────────────────────────────────┐
│     Histogram Background Subtraction     │
└─────────────────────────────────────────┘
┌─────────────────────────────────────────┐
│         Generation of DD/AA              │
└─────────────────────────────────────────┘
┌─────────────────────────────────────────┐
│        Bleedthrough Subtraction          │
└─────────────────────────────────────────┘
┌─────────────────────────────────────────┐
│       Application of Fc Threshold        │
└─────────────────────────────────────────┘
┌─────────────────────────────────────────┐
│    Fc/AA Calculation and Thresholding    │
└─────────────────────────────────────────┘
┌─────────────────────────────────────────┐
│         Scatter Plot Generation          │
└─────────────────────────────────────────┘
┌─────────────────────────────────────────┐
│          $E_{FRET}$ Calculation          │
└─────────────────────────────────────────┘
┌─────────────────────────────────────────┐
│    Application of Masks (VinTS Samples   │
│                 Only)                    │
└─────────────────────────────────────────┘
```
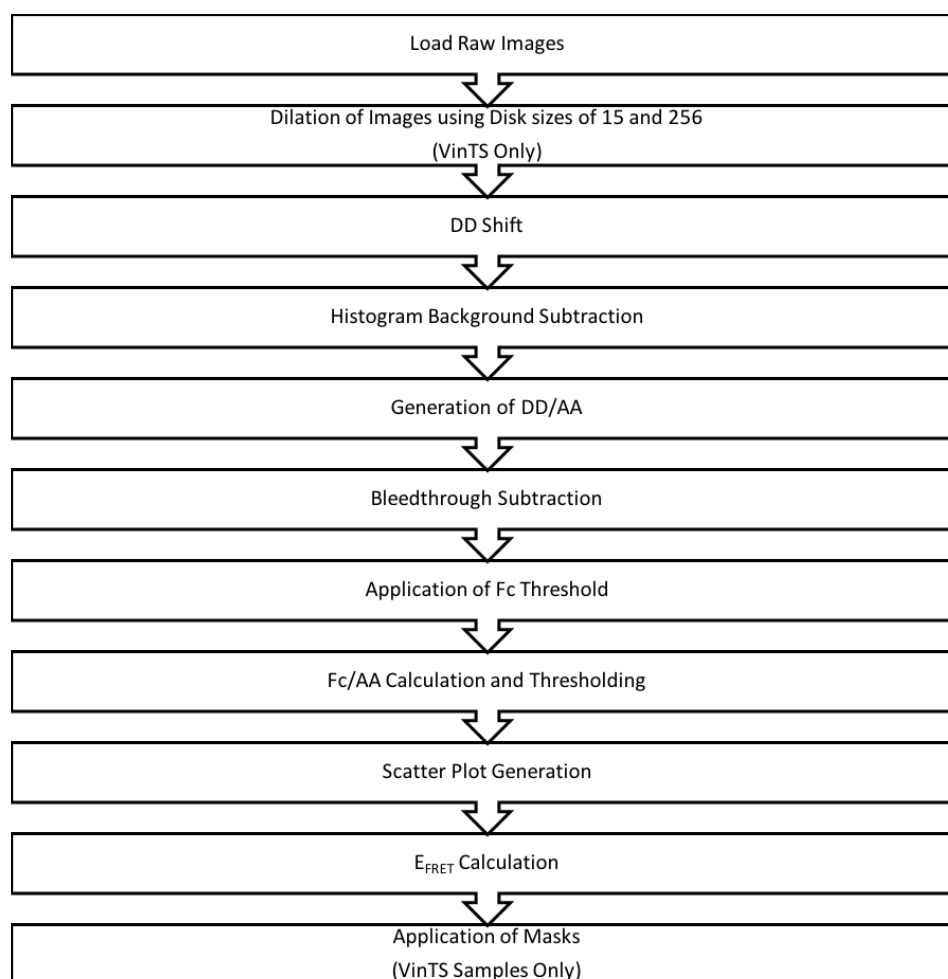
Figure 13: Overview of FRET Processing Method for iBMK and BAEC Samples

The fluorescence of the culture is normally sufficiently visible within 1 to 2 days, the cells are imaged, as described in Chapter 1. It was also noted that a specific methodology was created for each tested classification. Both the iBMK and BAEC lines were processed in the same way, as they both have similar cell shape.

2.2: Trials in Immortalized Baby Mouse Kidney Epithelial Cells

2.2.1: An Overview of Immortalized Baby Mouse Kidney Epithelial Cells

The immortalized Baby Mouse Kidney Epithelial (iBMK) cell line is derived by the co-expression of adenovirus E1A and dominant-negative p53 (p53DD). [39] Once the cell line is derived it can be aliquoted then frozen and stored for extended periods of time. The cells, once thawed, were grown in a 25 cm^2 culture flask from which cells were taken for platting. When in culture, the iBMK cell line is incubated at 38°C with an 8.5% CO_2 concentration, with splits occurring every 3-4 days when it reaches 80-90% confluence.

2.2.2: Calibration in Immortalized Baby Mouse Kidney Epithelial Cells

As discussed in Chapter 1, four constructs were transfected into iBMK samples. Each of these constructs served to allow for calibration of the system. The Donor Only (mTFP1) and Acceptor Only (mVenus) constructs were utilized for the calculation of their respective Bleedthrough values. The calculated Donor Bleedthrough value was 0.660 and the calculated Acceptor Bleedthrough value was 0.449. These values were found by first imaging the transfected constructs in our setup using 3-channel Sensitized Emission. These images were then processed using the linear regression method described in Chapter 1.3.1 and averaging the ob tained values. (See Table 1)

	iBMK Bleedthrough	
	mTFP (Donor)	mVenus (Acceptor)
	0.686	0.465
	0.699	0.467
	0.653	0.432
	0.670	0.458
	0.665	0.429
	0.652	0.453
	0.653	0.424
	0.673	0.450
	0.653	0.461
	0.666	0.458
	0.656	0.446
	0.646	0.450
	0.640	0.453
	0.654	0.445
	0.646	
	0.649	
Average	0.660	0.449
Standard Deviation	0.016	0.013

Table 1: Donor and Acceptor Bleedthrough Values for iBMK Samples

Once these values were obtained, we were able to use the aforementioned

MATLAB processing method to obtain the necessary components of the G Factor

equation. These included the F_c/AA and DD/AA values for our long and short linker

constructs. To do this we imaged samples transfected with the TRAF and (GGSGGS)$_2$

plasmids using the 3-channel Sensitized Emission methodology. We obtained a total of

26 sets of (GGSGGS)$_2$ images and 27 sets of TRAF images. The F_c/AA and DD/AA

values for each construct, shown in Table 2 and 3, were averaged then used to calculate

the G Factor for the iBMK cell line, which was 2.088. Since the total data set that was

used to calculate this value, was obtained by different users in 2 different sets, there is

confidence in this value being correct. The G Factors for each of these sets were 2.107

and 2.108. In addition, a comparison of the same image processed with G Factors of 2, 2.05, and 2.1 showed that the difference in E_{FRET} was insignificant, and in fact that an over estimation of the G Factor was the more conservative option. This conclusion is used later on when processing VinTS samples.

	iBMK (GGSGGS)2 Samples		
	Fc/AA	DD/AA	Efficiency
	1.691	0.693	0.539
	1.556	0.543	0.579
	1.968	0.667	0.586
	1.956	1.165	0.446
	2.132	0.903	0.531
	2.285	1.271	0.463
	2.085	1.014	0.496
	1.981	0.957	0.498
	2.291	1.125	0.494
	2.348	1.281	0.467
	1.973	1.015	0.482
	1.716	0.814	0.503
	2.276	1.183	0.480
	2.331	1.086	0.507
	2.229	1.077	0.498
Average	2.055	0.986	0.499
Standard Deviation	0.251	0.224	0.040

Table 2: Fc/AA, DD/AA, and E_{FRET} Values for iBMK (GGSGGS)$_2$ Linker Samples

	iBMK TRAF Samples		
	Fc/AA	DD/AA	Efficiency
	0.422	1.512	0.118
	0.178	2.045	0.040
	0.172	1.747	0.045
	0.244	2.159	0.051
	0.052	2.050	0.012
	0.291	1.917	0.068
	0.154	1.488	0.047
	0.236	1.776	0.060
	0.191	2.142	0.041
	0.176	1.648	0.049
	0.245	2.186	0.051
	0.201	1.905	0.048
	0.158	1.518	0.048
	0.224	2.076	0.049
`	0.318	1.821	0.077
Average	0.217	1.866	0.053
Standard Deviation	0.085	0.245	0.023

Table 3: Fc/AA, DD/AA, and E_{FRET} Values for iBMK TRAF Linker Samples

As seen in Table 2 and Table 3, the calculated E_{FRET} for the TRAF construct ranged from 0.03 to 0.06 and the calculated E_{FRET} for the (GGSGGS)$_2$ construct ranged from 0.47 to 0.49. The F_c/AA and DD/AA values obtained from the constructs were plotted on a scatter plot. (Figure 14) It can be seen that the values obtained for each construct form distinct clouds. By finding the average value for the TRAF and (GGSGGS)$_2$ datasets, which are located in the center of each cloud, and plotting a line between them. The slope of this line is equal to the negative of the G Factor. This graphical representation serves as an empirical validation to the mathematical approach described in Chapter 1 using Equation 2. [37] Further validation for this method is evident in the fact that the G Factor obtained with this linear slope method matches the mathematically calculated G Factor. This method also serves to allow the observer to visualize the distribution of the data.
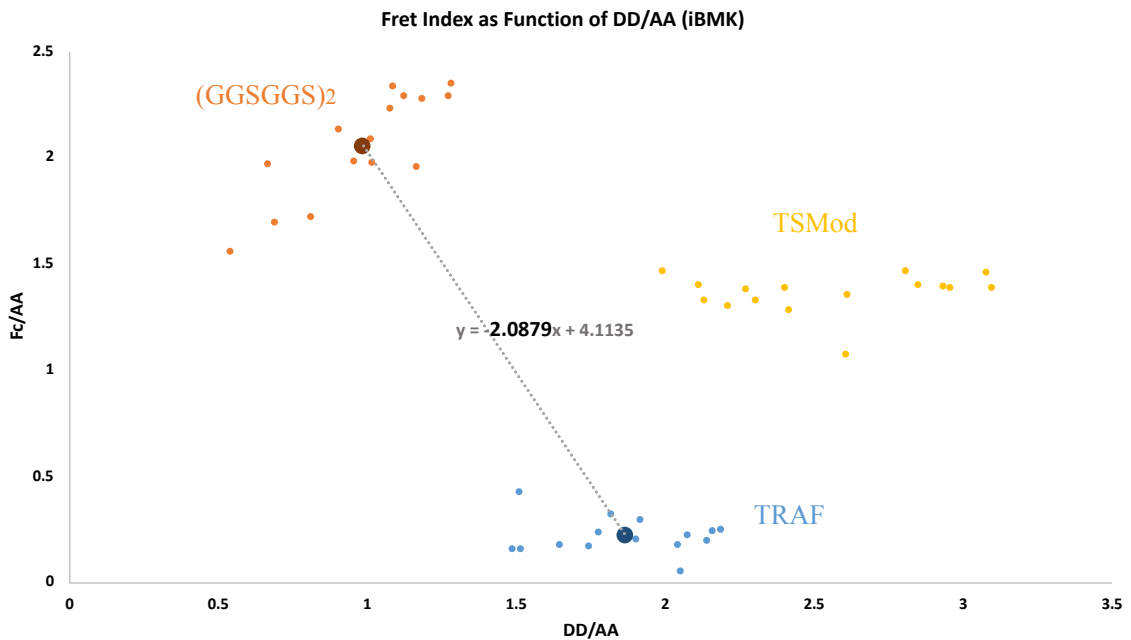
Figure 14: FRET Index as a Function of DD/AA for iBMK Samples

The TSMod construct within the iBMK data is also seen in Figure 14. This data was obtained several months after the TRAF and (GGSGGS)$_2$ data shown in the plot. The offset of this dataset, particularly along the x-axis or DD/AA direction, is discussed later on, but the values obtained from it matter nonetheless. The calculated E_{FRET} values for the TSMod construct had an average of 0.204, which is lower than the expected value 0.286. This can most likely be attributed to the DD/AA skew, as the Fc/AA values observed, and shown in Figure 14, do fit between the other two control constructs. This is key in the analysis, as it means that the E_{FRET} for that construct should fall between the two extremes. An optimization of how to reduce this skew is discussed in Chapter 4, along with other future directions of study.

	iBMK TSMod Samples		
	Fc/AA	DD/AA	Efficiency
	1.468	2.807	0.200
	1.329	2.303	0.216
	1.328	2.128	0.230
	1.386	3.097	0.177
	1.389	2.955	0.184
	1.287	2.416	0.203
	1.469	1.991	0.261
	1.405	2.850	0.191
	1.396	2.930	0.186
	1.358	2.609	0.200
	1.304	2.210	0.220
	1.460	3.077	0.185
	1.404	2.112	0.242
	1.388	2.400	0.217
	1.071	2.605	0.165
	1.385	2.271	0.226
Average	1.364	2.547	0.204
Standard Deviation	0.095	0.367	0.026

Table 4: F_C/AA, DD/AA, and E_{FRET} Values for iBMK TSMod Samples

2.2.3: Measurement in Immortalized Baby Mouse Kidney Epithelial Cells

     Images of the VinTS construct were able to be obtained, with isolated fluorescence within the Focal Adhesions. As described in Figure 15, selective procedures were reserved for VinTS samples. These procedures were designed to allow for isolation of the Focal Adhesions within the iBMK line.
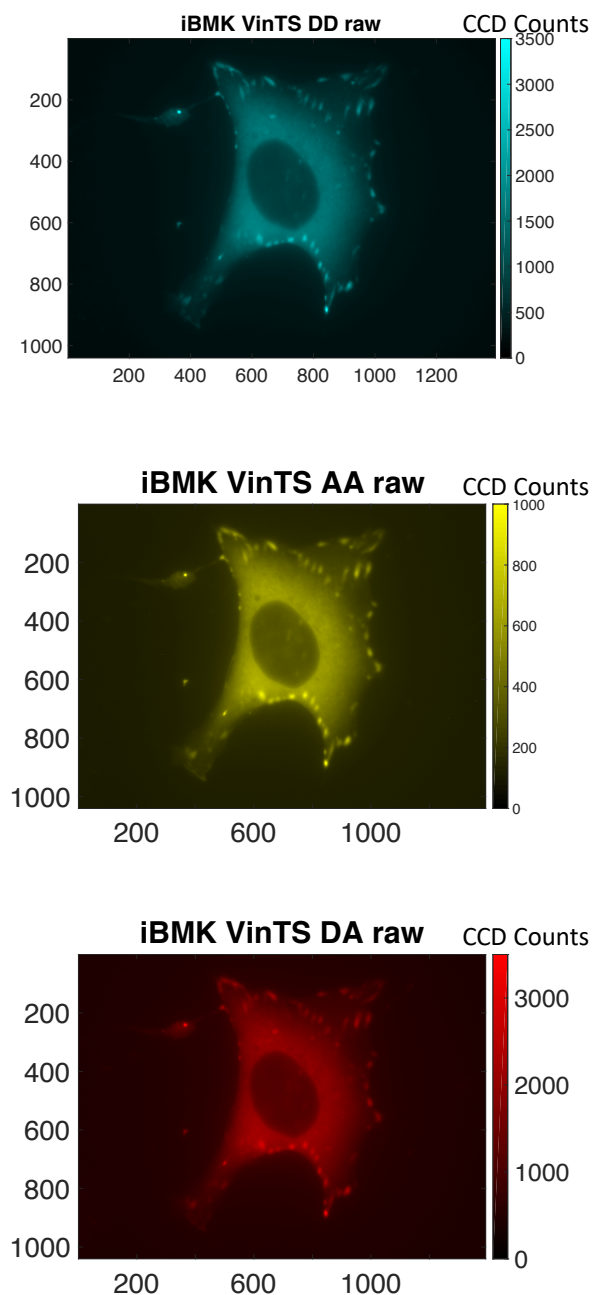
Figure 15: Raw 3-Channel Sensitized Emission iBMK Images with Monochrome Coloration
(Field of View: 90 μm by 70 μm)

After raw images are obtained, a dilation operation is performed on the DA image using disks of two sizes. The first disk had a radius of 15 pixels and was used to isolate the Focal Adhesions within the cell. The second disk had a radius of 256 pixels and was used to isolate the cell as a whole. The results from both of these dilations operations produced two masks that were applied to the processed image to isolate the Focal Adhesions or entire cell, respectively.
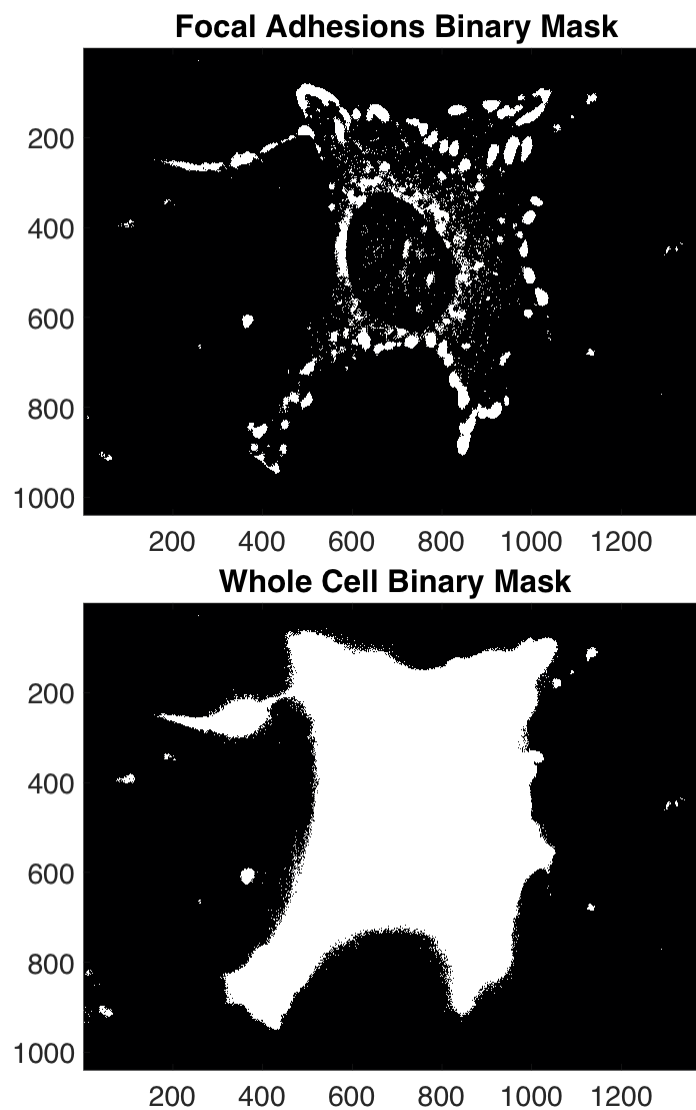
Figure 16: Masks used for Processing of Raw iBMK Cells shown in Figure 15
(Field of View: 90 μm by 70 μm)
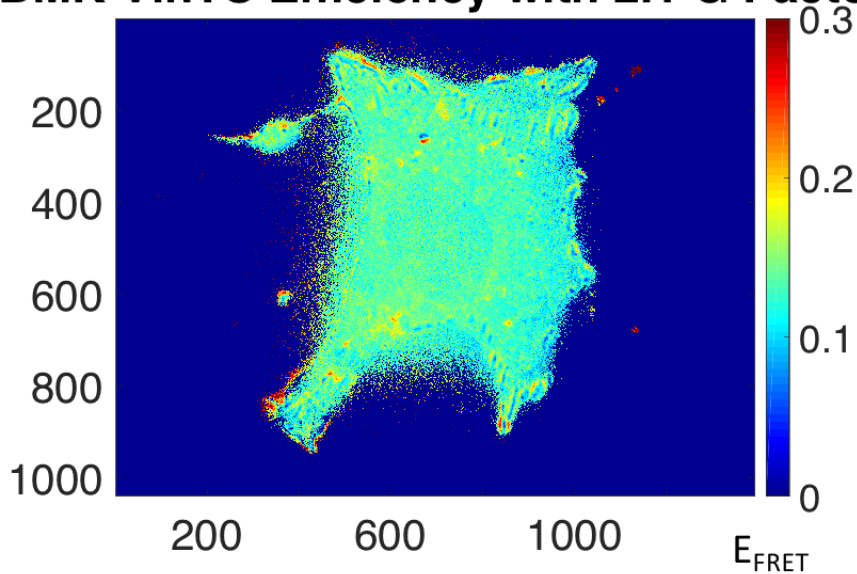
Figure 17: Processed Image of an iBMK Cell before masking
(Field of View: 90 μm by 70 μm)
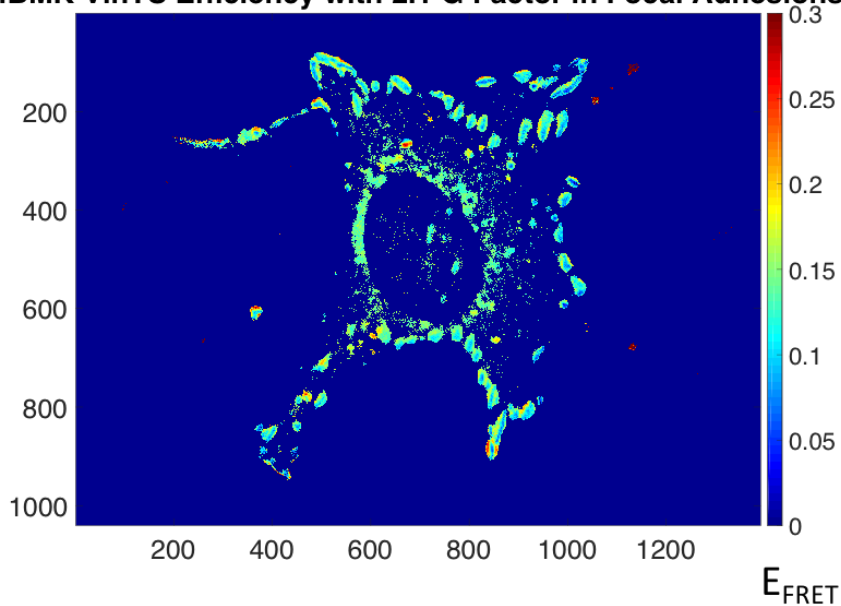
Figure 18: Processed Image of an iBMK Cell after masking
(Field of View: 90 μm by 70 μm)

2.3: Trials in Bovine Aortic Endothelial Cells

2.3.1: An Overview of Bovine Aortic Endothelial Cells

Bovine Aortic Endothelial Cells (BAEC) are obtained directly from slaughtered cattle that are inspected by the USDA and considered healthy. They are delivered aliquoted and ready for extended cryopreservation in liquid nitrogen. When they are thawed and placed into culture, they are incubated at 37°C and a 5% CO_2 concentration. They are limited in the number of passages that they can be split to before their health begins to decline. This is because the cells, as opposed to the aforementioned iBMK cell line, are not immortalized and therefore age. This limits the timeframe during which experiments can be conducted with the thawed cells. This additional consideration must be kept in mind when working with them, including how the data obtained from them at later stages is analyzed and interpreted, as variations can be introduced due to aging.

2.3.2: Calibration in Bovine Aortic Endothelial Cells

The measured Bleedthrough values for the BAEC line was similar to that of the iBMK line, with a Donor Bleedthrough of 0.671 and an Acceptor Bleedthrough of 0.464. These Bleedthrough values were obtained in the same way as the iBMK samples and are shown in Table 5.

	BAEC Bleedthrough	
	mTFP (Donor)	mVenus (Acceptor)
	0.670	0.504
	0.658	0.428
	0.669	0.421
	0.669	0.433
	0.661	0.429
	0.696	0.441
	0.673	0.432
	0.666	0.454
	0.664	0.430
	0.681	0.551
	0.676	0.523
	0.655	0.518
	0.685	0.455
	0.676	0.471
	0.673	0.473
	0.672	0.455
	0.670	
Average	0.671	0.464
Standard Deviation	0.010	0.040

Table 5: Donor and Acceptor Bleedthrough Values for BAEC Samples

	BAEC (GGSGGS)2 Samples		
	Fc/AA	DD/AA	Efficiency
	2.274	1.089	0.499
	2.201	1.170	0.473
	2.006	0.830	0.536
	2.155	1.230	0.456
	1.505	1.023	0.413
	2.585	1.248	0.497
	2.555	1.266	0.491
	2.184	0.974	0.517
	2.265	0.998	0.520
	1.849	1.157	0.433
Average	2.158	1.098	0.484
Standard Deviation	0.318	0.141	0.040

Table 6: Fc/AA, DD/AA, and E_{FRET} Values for BAEC (GGSGGS)$_2$ Linker Samples

	BAEC TRAF Samples		
	Fc/AA	**DD/AA**	**Efficiency**
	0.153	1.665	0.042
	0.319	1.731	0.081
	0.418	1.762	0.102
	0.365	2.255	0.072
	0.352	2.330	0.067
	0.194	2.667	0.034
	0.108	1.435	0.035
	0.486	2.047	0.102
Average	0.299	1.986	0.067
Standard Deviation	0.134	0.411	0.028

Table 7: F_C/AA, DD/AA, and E_{FRET} Values for BAEC TRAF Linker Samples
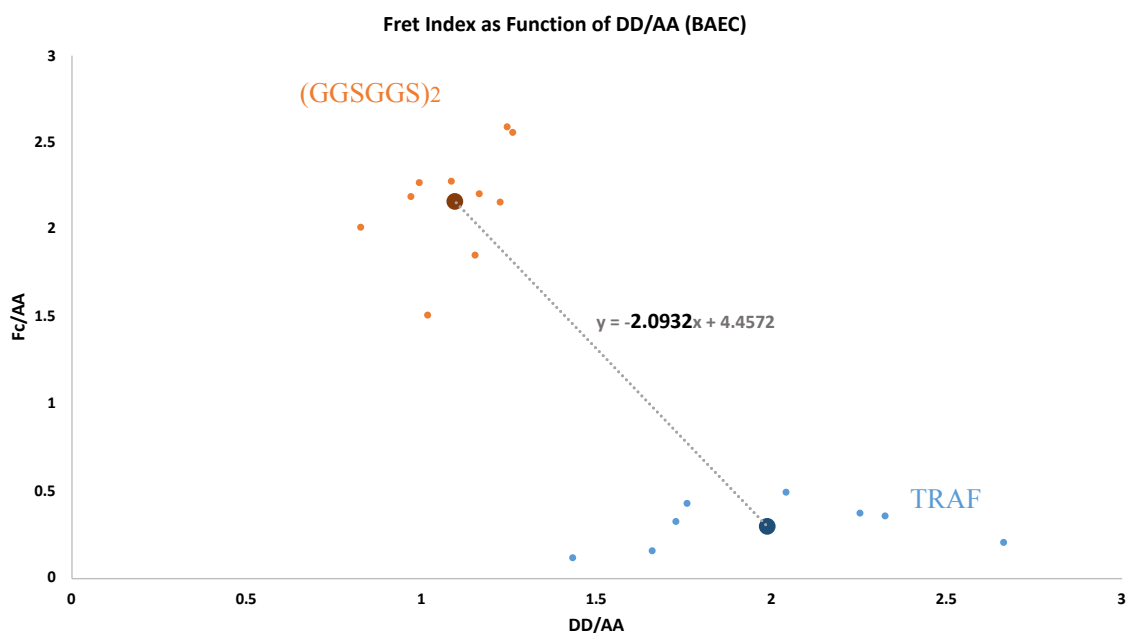
Figure 19: FRET Index as a Function of DD/AA for BAEC Samples

Similar to the data obtained from the iBMK cell line, the F_c/AA and DD/AA data

from the BAEC line was plotted on a scatter plot. This data can be seen in Table 6 and

Table 7. The G Factor calculated using the both the slope approach and the analytical

Equation was 2.093. The E_{FRET} samples were also similar to that of the iBMK samples,

with the E_{FRET} for the TRAF construct ranging from 0.01 to 0.11 and the E_{FRET} for the

(GGSGGS)$_2$ ranging from 0.41 to 0.53.

2.3.3: Measurement in Bovine Aortic Endothelial Cells

Expression of the VinTS construct within the BAEC line was successful. Images

of the construct being expressed by the line are shown here. The images were obtained

and processed in the same way as those of the iBMK line. An example image is shown in

Figures 20 through 23, as it is processed using the same method as the iBMK samples.
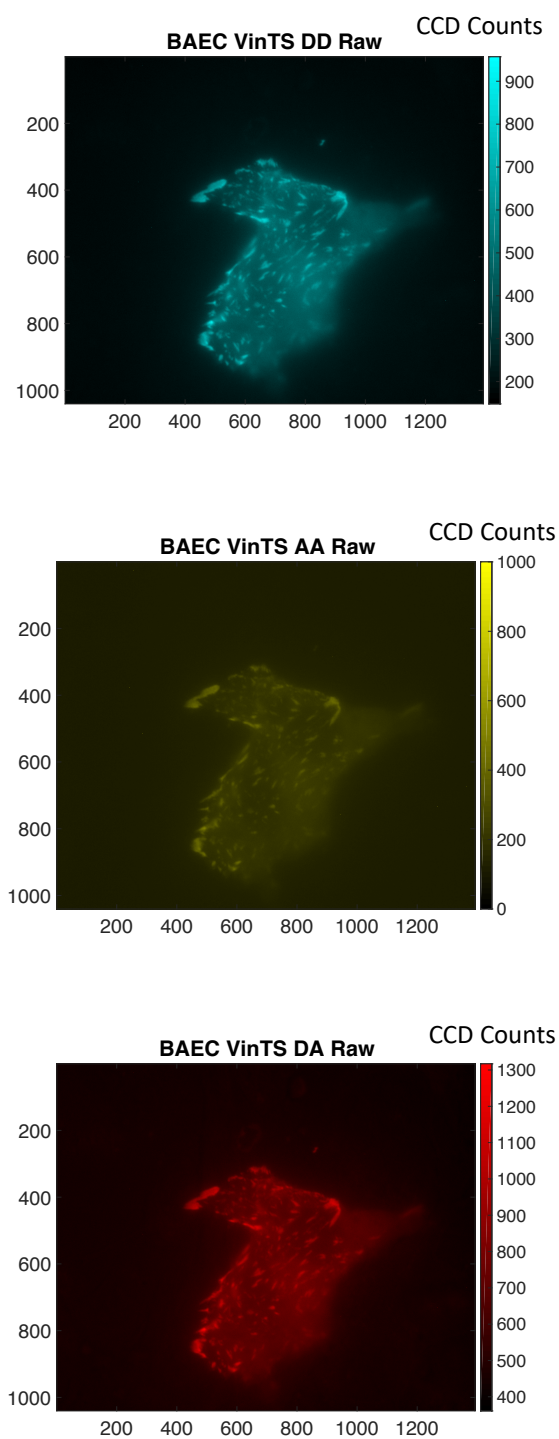
Figure 20: Raw 3-Channel Sensitized Emission BAEC Images with Monochrome Coloration
(Field of View: 90 μm by 70 μm)

Focal Adhesions Binary Mask

Whole Cell Binary Mask
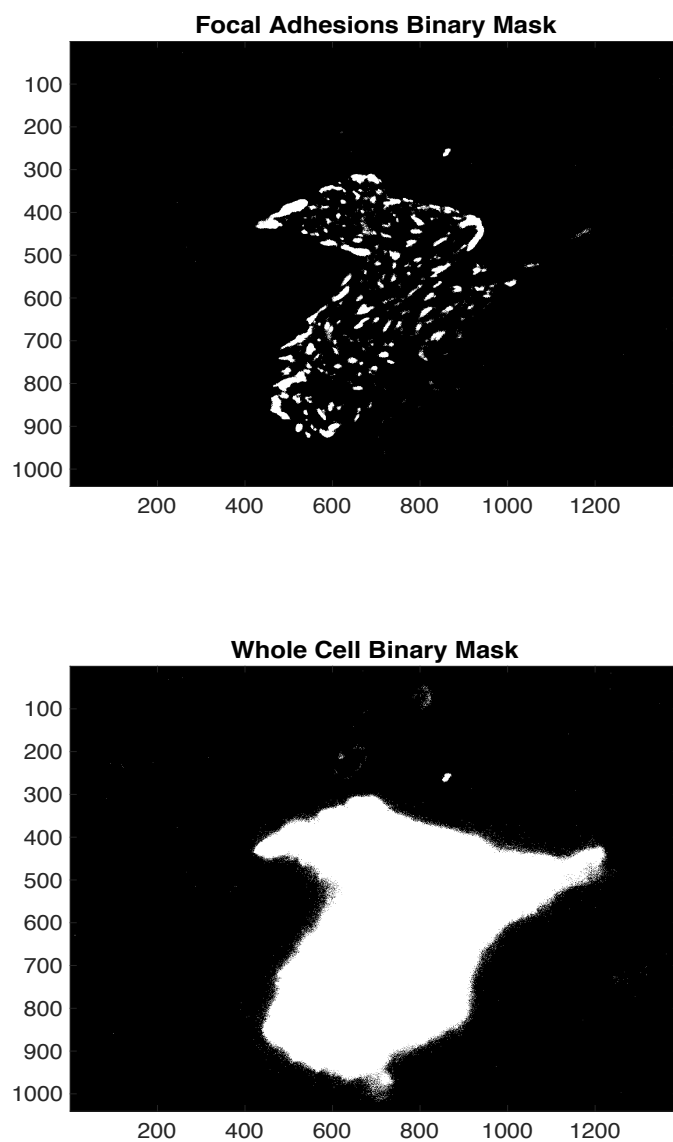
Figure 21: Masks used for Processing of Raw BAEC Cells shown in Figure 20
(Field of View: 90 μm by 70 μm)
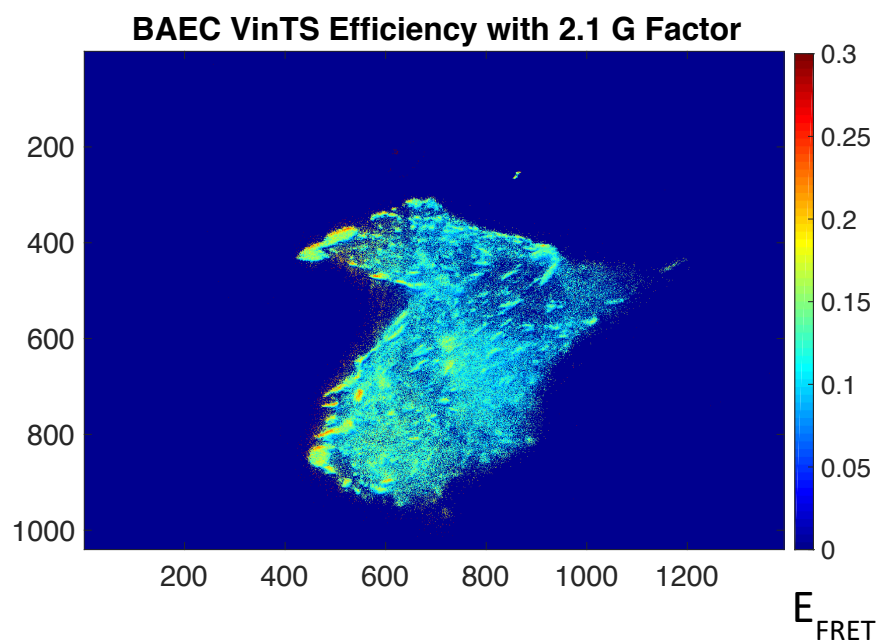
Figure 22: Processed Image of a BAEC Cell before masking
(Field of View: 90 μm by 70 μm)
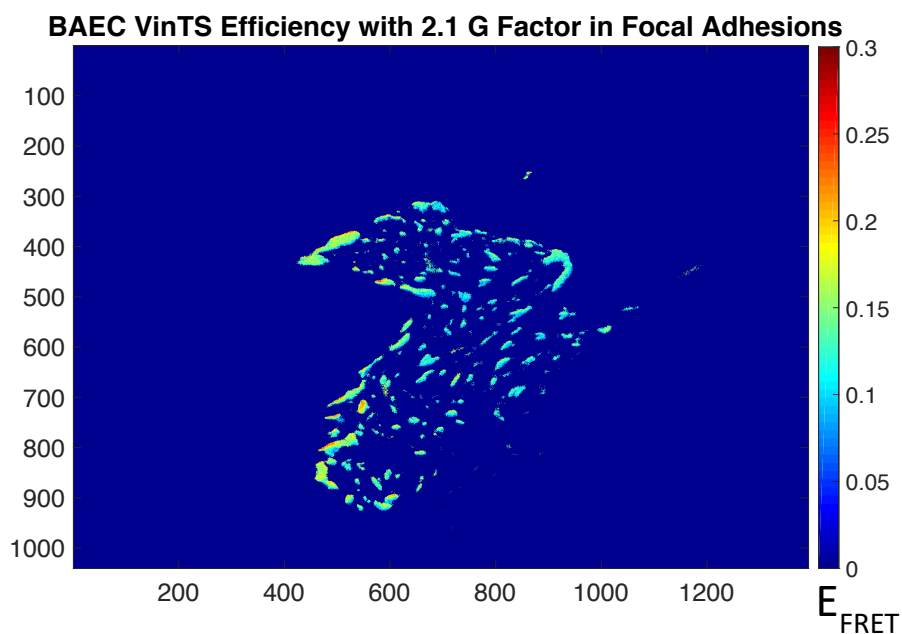
Figure 23: Processed Image of a BAEC Cell after masking
(Field of View: 90 μm by 70 μm)

2.4: Discussion of iBMK and BAEC Results

The results from the iBMK and BAEC line samples were very promising. The E_{FRET} values for both soluble Linker control constructs, in both of the cell lines were consistent with literature. For the TRAF construct, an E_{FRET} of less than 0.11 is to be expected. [16] This is mainly due to the large distance that is present with the TRAF linker, as well as the fact that TRAF forms a trimer which causes its E_{FRET} not to be perfectly well defined. For the $(GGSGGS)_2$ construct, several published literature sources place the expected E_{FRET} in the range of approximately 0.23 to 0.4.[29] The E_{FRET} of our construct is expected to be approximately 0.5. This value is higher than what the linker has produced in the past, as the new linker has had extras residues removed. [40]

The images of the iBMK and BAEC line successfully show the expression of the VinTS construct within Focal Adhesions, allowing for their isolation and the measurement of E_{FRET} within them. The values observed, however, differ from published literature. The E_{FRET} observed in cells of similar type was approximately 0.242.[29] This differs from the values observed in the iBMK and BAEC lines, which are around the 0.15 to 0.2 range. The distance from the cells center should be considered, as it has been should that lower E_{FRET} is observed near cell edges and far from the cell center.[29] For the iBMK line, many of the measured Focal Adhesions are far from the cell center, so a lower E_{FRET} is not unexpected. While the consistent distribution of the E_{FRET} in the BAEC line did appear unusual a first, expression of the construct in a different line could produce distinct results. The consistency of the measurements over time and in different sets are what determine the accuracy of the method.

The repeatability and consistency of isolation is based in the ability of the Focal Adhesions to be isolated using the dilation operation of proper disk size that generates the mask. The generation of the mask to isolate the areas is the basis of how the isolation occurs. By generating a mask that can isolate the Focal Adhesions, the cell body and other areas can be eliminated using a simple multiplication operation. The consistency in the size of the Focal Adhesions also plays a role in this.

The similarity of the G Factors obtained from both cell types was expected, as the G Factor is setup dependent, not cell dependent. A minor difference between the two calculated values was anticipated, as expression variability was expected. The transfection efficiency, however, was anticipated to be more uniform. Efficiencies of approximately 40% throughout testing were observed between the two cell lines. In addition, as discussed earlier on, small variations of the G Factor can occur within a single cell type. This variation was shown to be insignificant and that an overestimation of the G Factor properly accounts for it.

CHAPTER 3: CALIBRATION AND MEASUREMENT IN NEURONS

Within the biological community, understanding how neurons interact with their environment, including the forces that affect them, is an area of great interest. This is due to the observation that there are differences in mechanical stiffness of brain tissue in a variety of neuronal conditions, including injury and neurodegenerative conditions.[41, 42] In addition, there is evidence that mechanical forces impact neuronal growth and development. Specifically, studies have shown that the neuronal cytoskeleton interacts with the ECM to promote extension of Growth Cones, which are found on the end of neuronal processes.[43] Neurogenesis is of particular interest, due to extensive nature of cellular interactions with their environment. These interactions can greatly affect development, and better understanding them could provide great insight into how the nervous system forms.[44] This area is also of great interest because the cells here undergo mechanotransduction, or the translation of physical force to chemical signals, and therefore undergo a physical force that may be able to be measured.

Since the VinTS probe is able to be expressed and measured in a variety of cell types, it is a potential tool for force measurement in neurons. It has been previously studied in a variety of cell types including fibroblasts epithelial cells, but has not be tested in neurons.[25, 37] This is intriguing as the behavior of neurons during growth and development is an optimal area for use of the VinTS probe. This is due to the extensive occurrence of neurogenesis, and therefore a plethora of Growth Cones. The probe can allow for visualization and localization of forces, as well as quantify the forces that the area is undergoing. This is possible as the Vinculin protein is located within developing neurons, particular in the neuronal Growth Cone area.[44]

3.1: A Background on Neurons and their Associated Properties

3.1.1: A Biological Overview of the Selected Neuron Cell Type

There are a variety of neurons that fall into several classifications. One type that will allow for better understanding neuronal development is the cortical neuron. These are the neurons of the Cerebral Cortex, and they are generated in the ventricular zone, which is also where neuronal stem cells develop. [45] The proximity of cortical neurons during embryonic development make them an optimal candidate for study. For this reason, Isolated Cortical Neurons were the cell type utilized in this study. Young developing neurons exhibit behavior that is desirable for study, particularly the display of Growth Cones. Growth Cones, as mentioned earlier, are found on the end of extending neuronal processes and also contain the Vinculin protein.[44] It is also understood that the protein can be found in other areas of the neuron, including throughout neuronal processes and branching points, that do not end at a Growth Cone. The construct, upon transfection, can then be visualized within these areas.

3.1.2: Harvest and Preparation for Testing

The Isolated Cortical Neurons utilized for study were obtained from the lab of Dr. Bonnie Firestein. The cells are harvested from fetal rat on embryonic development day 18 (E18). They are plated on coverslips that were prepared in a similar way to the coverslips used for the iBMK and BAEC cultures. The difference arises in the need for a coating of the coverslips to allow for cellular adhesion. This is needed, as neurons cannot grow directly on glass and require the presence of certain chemical treatments for proper cellular adhesion.

After the coverslips have been cleaned, a Poly-D Lysine (PDL) coating is applied to the coverslips. This involves the mixing of a stock Borate Buffer with the stock PDL solution. Each well is then filled with 1mL of the mixed solution, left overnight in the coating solution, then washed using Sterile Deionized Water. This is done by aspirating the solution from each well and filling each well with 1 mL of the Sterile Water. The water is then left for 15 minutes in the wells. This procedure of aspiration and filling is repeated two more times. The third wash is only aspirated before filling with a prepared Laminin Solution, prepared by mixing another portion of Borate Buffer with a Laminin stock. Once the coverslips have been aspirated and filled with 1 mL of the Laminin solution, it is again left to soak overnight. The coverslips are then washed using the Sterile Water in the same way as before; aspirating and filling 3 times. After the third filling with Sterile Water the plate is brought to the collaborator's lab to plated. The platting density, and therefore culture density, for all of the neuronal cultures was 50,000 cells/cm^2. Each 12-well well is 4cm2.

The culture medium for the neurons is different from that of the BAEC and iBMK. The medium used is Neurobasal Medium, which is modified in lab. The medium is composed of 48.5 mL of stock Neurobasal medium along with 1mL of B27 and 0.5mL Glutamax. Half of the medium that the culture is in is replaced every 3-4 days that the neurons are in culture. This is done by removing all medium and putting it aside, then replacing each culture with half of the saved medium and half of new lab-made medium.

3.1.3: Implementation of Protocols

The neuronal cultures were transfected in a similar way to the iBMK and BAEC cultures. This was through a Lipofectamine® LTX plasmid insertion protocol. The date of transfection is also important. Transfection occurred on DIV 4-7, as this was the optimal time to visualize the areas of interest within the cells. The volumes utilized for this protocol were adjusted to optimize transfection success and cell viability after transfection. The adjusted volumes can be seen in Figure 24.

	Prepare Cells and Plate them in Culture
Lipofectamine Tube: • 100 µL OPTI-MEM • 2 µL Lipofectamine® LTX Stock DNA Tube: • 100 µL OPTI-MEM • 3 µL DNA Stock • 1.5 µL PLUS™ Reagent	Prepare Lipofectamine® LTX and DNA Solutions for each Plasmid using OPTI-MEM® Medium
5 min	Allow Solutions to sit for 5 minutes
	Transfer Prepared DNA Plasmid Solution into Lipofectamine® LTX Solution
25 min	Wait for 25 minutes
	Add Mixed Solution to culture

Figure 24: Overview of the Adjusted Neuron Lipofectamine® LTX Transfection Procedure

In addition to the difference in solution volumes that make up the Lipofectamine® LTX-DNA Mixture, the procedure for incubation differs. For the neuronal cultures, the culture medium is saved and set aside before the addition of the Mixture. The culture is incubated in new Neurobasal Medium. The culture is also only incubated for 1 hour, before the incubation medium is aspirated and replaced with half

new and half saved Neurobasal medium. Neuronal cultures remain transfected for a

longer period of time, allowing more time to image the sample, as the cells do not divide.

Image acquisition is the same for neuronal cultures, but the neurons do require a

modified processing method, due to their different cellular structure, compared to the

iBMK and BAEC lines. This process is shown in Figure 25.

Load Raw Images
DD Shift
Cell Isolation (SCIRD-TS)
Pixel Binning and Averaging
Histogram Background Subtraction
Application of Threshold on all Images
Generation of DD/AA
Bleedthrough Subtraction
Application of Fc Threshold
Fc/AA Calculation and Thresholding
Scatter Plot Generation
E_{FRET} Calculation
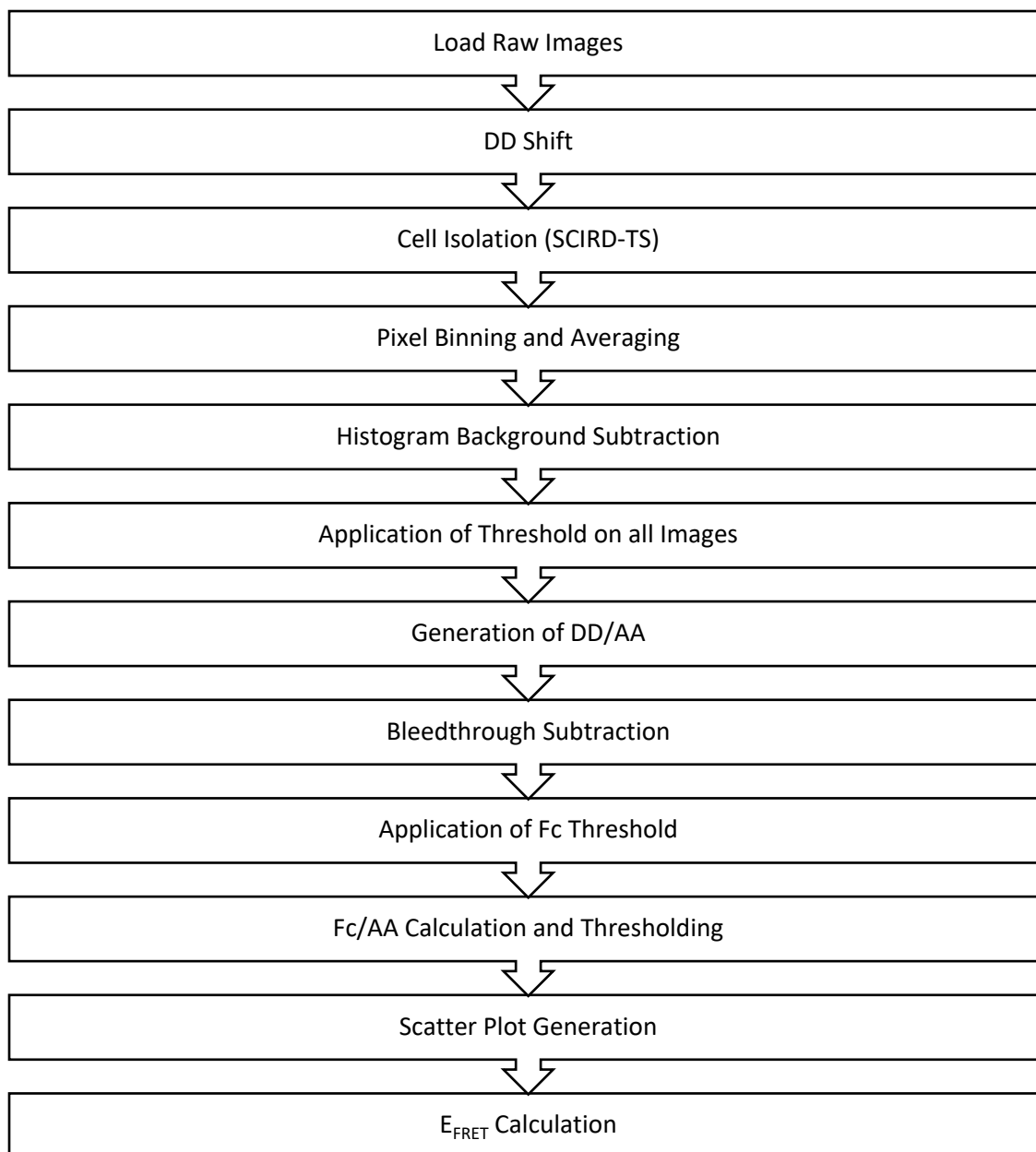
Figure 25: Overview of the Neuron Image Processing Procedure

The most significant difference between the Neuronal Processing Code and the code used to process the iBMK cells is the image isolation method. For the neuronal samples, a ridge detection algorithm called Scale and Curvature Invariant Ridge Detector for Thin Structures (SCIRD-TS), is used. This method has been optimized to isolate thin structures and segment them.[46, 47] The base methodology, however, need to me modified to better fit our structure type. This is due to the base SCRID-TS code being created for medical imaging and structures. The plethora of input parameters required fine tuning to best isolate the neurons and their processes are explained in Table 8.

Overview of SCIRD-TS Parameters		
Parameter	Meaning	Value Used
Input Parameters		
I	Input Image	N/A
Ridges Color	Specifies if structures are Black or White	
Filter Bank Input Parameters		
Alpha	Controls the balance between contrast and filter bank response. Used if structures of interest are not contrasted well.	0
Sigma 1	Elongation Range	[3]
Sigma 1 Step	Step used to span Sigma 1 Range	1
Sigma 2	Width	[2 3]
Sigma 2 Step	Step used to span Sigma 2 Range	1
K	Curvature Range	[-0.1 0.1]
K Step	Step used to span K range	0.025
Filter Size	Sets width and height of each filter	25
Angle Step	Step used to span 180°	12
Output		
outIm	Filtered Output Image	N/A
Properties	Contains parameters for each filter created	
ALLfiltered	Response of the SCRID-TS Filter Bank before Soft Thresholding and Contrast adaption	

Table 8: Overview of SCRID-TS Processing Input and Output Parameters

An additional processing step that was integrated into the processing of the neuronal samples involved the "Binning" of the pixels of the images after the shifting step. This process involved the grouping pixels into squares of 4 pixels by 4 pixels and replacing them with the mean value of those pixels. This technique allowed for both signal boosting and better isolation of areas of interest. This is done through the averaging operation that occurs; where pixels of high and low signal balance each other out. The isolation occurs due to the fact that the pixels which have been eliminated by threshold, and therefore set to 0, improve the clarity of the edges by reducing the average calculated in the area.

The Bleedthrough used to calculate F_C for the TRAF, (GGSGGS)$_2$, TSMod, and VinTS was the same as the iBMK cells. This was to maintain consistency between datasets and overcome the inherent unequal construct distribution within Neurons. When the Donor Only and Acceptor Only Constructs were imaged and their Bleedthrough measured, the values obtained were higher than expected. The obtained Donor Bleedthrough value was 0.694 and the Acceptor Bleedthrough value was 0.524. The calculated Bleedthrough should remain constant for all processing methods. This is because the values should be instrument dependent, not cell dependent. The iBMK values are chosen as they have been the most reproducible and consistent during testing.

3.2: Calibration in Neurons

After the completion of the aforementioned modified protocols, F_c/AA and DD/AA values were obtained and are shown in Table 9 and Table 10. The G Factor that was calculated using this data was 2.081, which is in line with the values obtained from

the iBMK and BAEC lines. This G Factor is used in the analytical calculation of the

E_{FRET} reported in Table 9 and Table 10.

Neuron (GGSGGS)2 Samples					
Fc/AA	DD/AA	Efficiency	Fc/AA	DD/AA	Efficiency
1.478	2.265	0.239	1.012	2.341	0.172
0.935	1.761	0.203	1.324	1.839	0.257
1.588	2.237	0.254	1.293	1.616	0.278
1.402	2.114	0.242	1.085	1.474	0.261
0.816	1.876	0.173	0.950	1.213	0.273
0.572	1.289	0.176	0.880	1.288	0.247
0.473	0.499	0.313	1.071	2.164	0.192
0.486	0.942	0.199	1.109	1.854	0.223
1.440	2.081	0.250	1.684	2.044	0.284
1.433	1.494	0.316	1.978	2.447	0.280
0.773	1.676	0.181	0.876	0.963	0.304
1.401	0.759	0.470	1.308	1.453	0.302
0.949	0.589	0.436	1.530	2.079	0.261
1.796	1.232	0.412	1.817	2.464	0.262
1.774	1.477	0.366	1.427	1.587	0.302
1.417	1.061	0.391	1.629	2.258	0.257
1.732	0.949	0.467	1.375	2.078	0.241
1.639	1.004	0.440	1.606	2.087	0.270
1.696	0.846	0.491	1.174	1.702	0.249
1.372	0.715	0.480	1.588	2.077	0.269
1.568	0.803	0.484	1.331	2.179	0.227
1.721	1.081	0.433	1.702	1.639	0.333
1.692	0.967	0.457	1.680	2.002	0.287
Average					
Fc/AA		DD/AA		Efficiency	
1.339		1.577		0.302	
Standard Deviation					
Fc/AA		DD/AA		Efficiency	
0.376		0.558		0.095	

Table 9: F_C/AA, DD/AA, and E_{FRET} Values for Neuron (GGSGGS)2 Linker Samples

Neuron TRAF Samples					
Fc/AA	DD/AA	Efficiency	Fc/AA	DD/AA	Efficiency
0.188	3.966	0.022	0.371	2.756	0.061
0.053	1.726	0.015	0.303	2.235	0.061
0.060	1.679	0.017	0.349	2.369	0.066
0.092	2.204	0.020	0.384	3.081	0.057
0.139	1.536	0.042	0.389	3.276	0.054
0.185	2.355	0.036	0.475	3.578	0.060
0.082	1.724	0.022	0.397	2.453	0.072
0.185	2.645	0.032	0.293	1.427	0.090
0.054	2.205	0.012	0.458	3.751	0.055
0.080	1.910	0.020	0.284	2.595	0.050
0.042	1.502	0.013	0.274	3.172	0.040
0.106	2.942	0.017	0.180	2.219	0.038
0.046	1.261	0.017	0.261	2.383	0.050
0.013	1.173	0.005	0.452	2.580	0.078
0.058	1.691	0.016	0.165	1.819	0.042
0.081	1.557	0.024	0.248	2.882	0.040
0.058	1.335	0.020	0.162	1.145	0.064
0.123	2.493	0.023	0.325	3.443	0.043
0.190	1.575	0.055	0.334	2.557	0.059
0.091	1.917	0.022	0.404	2.385	0.075
0.066	1.306	0.024	0.553	2.219	0.107
0.205	1.178	0.077	0.566	3.115	0.080
0.166	1.697	0.045	0.453	3.544	0.058
0.048	1.008	0.022	0.111	2.008	0.026
0.168	1.976	0.039	0.083	2.233	0.017
0.419	3.593	0.053	0.044	1.866	0.011
0.284	2.509	0.052	0.115	3.116	0.017
0.220	1.944	0.052	0.052	1.850	0.013
0.205	1.924	0.049	0.113	1.907	0.028
0.283	1.829	0.069	0.015	1.263	0.006
0.229	2.015	0.052	0.126	3.215	0.018
0.210	2.094	0.046	0.030	1.879	0.008
0.428	3.070	0.063	0.017	1.387	0.006
0.254	2.640	0.044	0.640	2.024	0.132
0.304	2.737	0.051	0.166	2.857	0.027
0.336	1.385	0.104			
Average					
Fc/AA		**DD/AA**		**Efficiency**	
0.216		2.238		0.042	
Standard Deviation					
Fc/AA		**DD/AA**		**Efficiency**	
0.153		0.719		0.026	

Table 10: Fc/AA, DD/AA, and E_{FRET} Values for Neuron TRAF Linker Samples

Fret Index as function of DD/AA (Neurons)

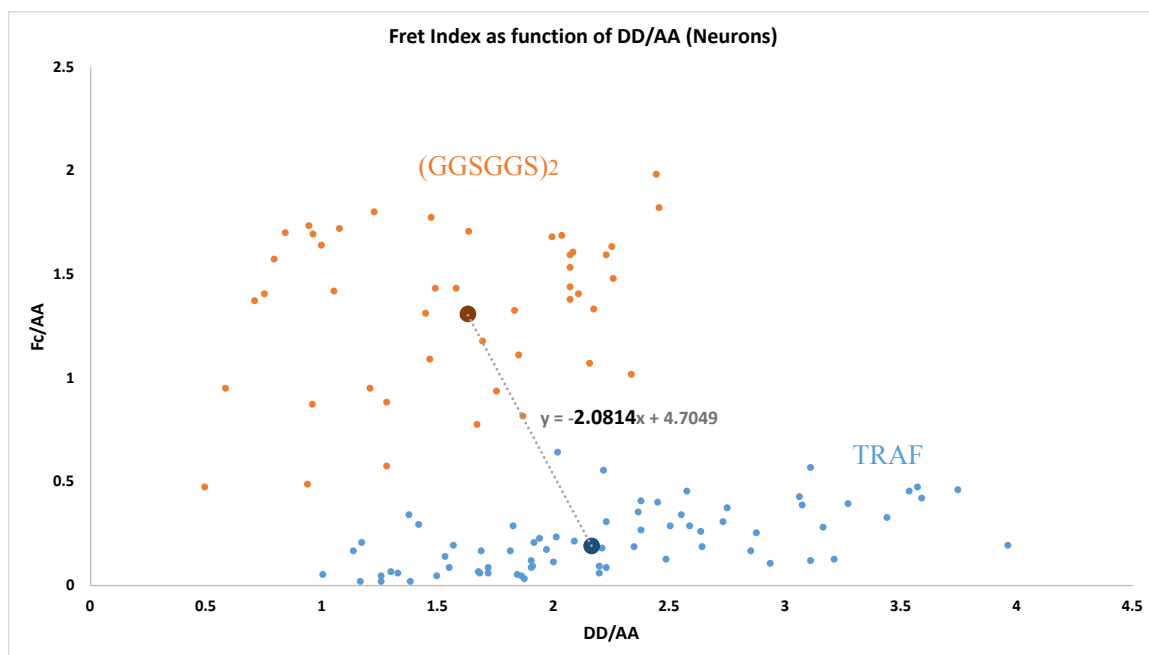$(GGSGGS)_2$

TRAF

$y = -2.0814x + 4.7049$

Figure 26: FRET Index as a Function of DD/AA for Neuron Samples

For the TSMod construct, overall image analysis was done. This meant that images were processed and then analyzed by looking at individual pixel values. A G Factor of 2.1 was used here again, as it is close to the calculated G Factor from the TRAF and $(GGSGGS)_2$ data. It also maintains consistency throughout all of the tested and processed cell lines, providing a proper basis for comparison.

As can be seen in Figure 27 below, an E_{FRET} in the range of 0.2 to 0.3 was observed in neurons transfected with TSMod. A lower E_{FRET} is seen in the center of the neurons, while a higher E_{FRET} is seen near the edges of the cells. Areas of high raw signal also appear to produce areas of low E_{FRET}. These are mainly the cell bodies, which are saturated. This means that the camera's ability to measure the signal has reaches its peak and cannot measure anymore signal. This issue was especially evident in the early trials, before power reduction. This will be discussed in more detail at the end of this chapter.
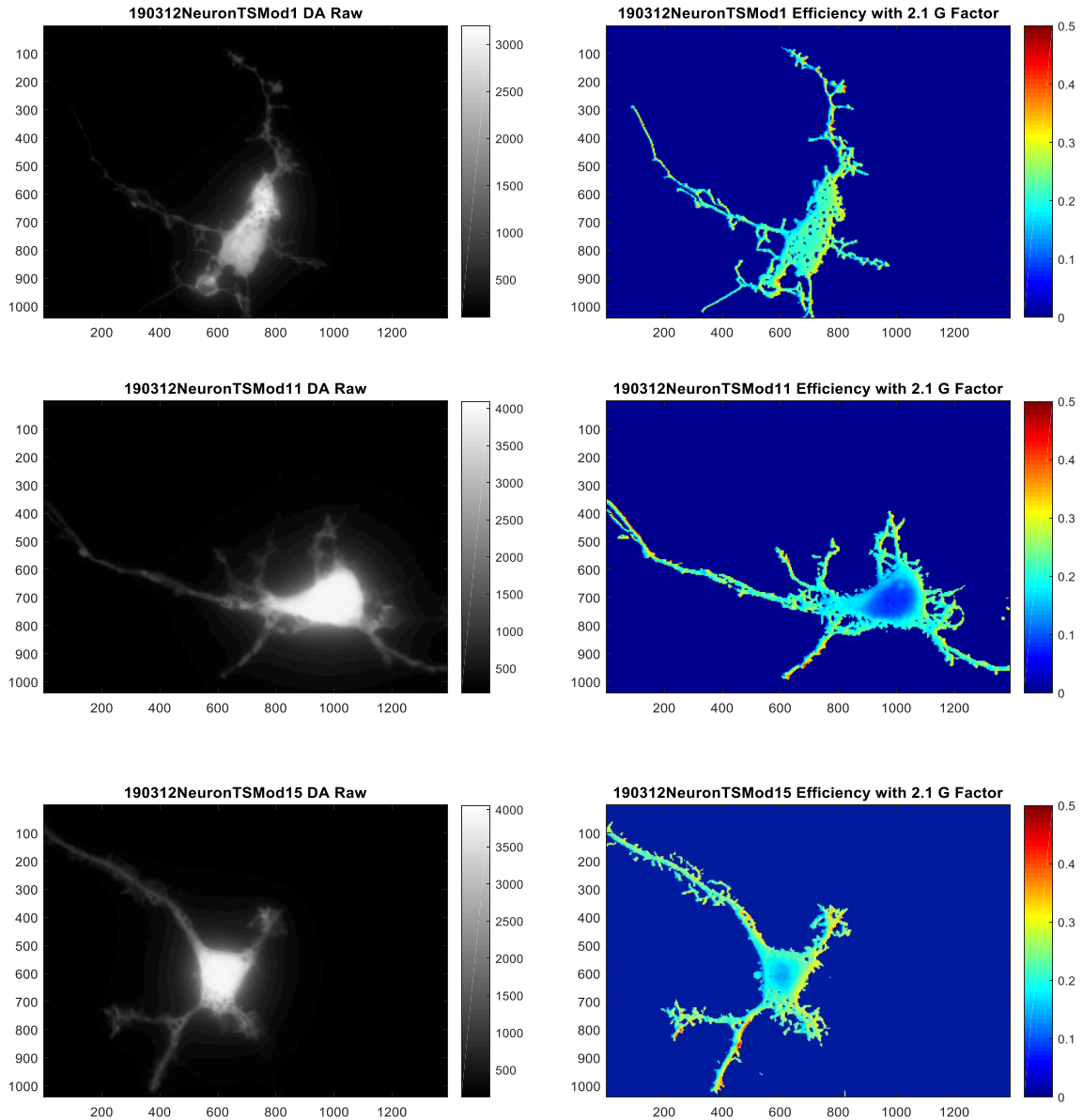
Figure 27: Processed TSMod Neurons displaying E_FRET throughout the cell
(Field of View: 90 μm by 70 μm)

3.3: Measurement in Neurons

Images of the VinTS construct within Neurons were obtained and processed using

the "binning" method with a G Factor of 2.1 and iBMK Bleedthrough values. The images

shown here demonstrate that the VinTS construct can successfully be expressed and

measured in neurons. The variability of the measured E_{FRET} throughout the cell and processes is also seen.
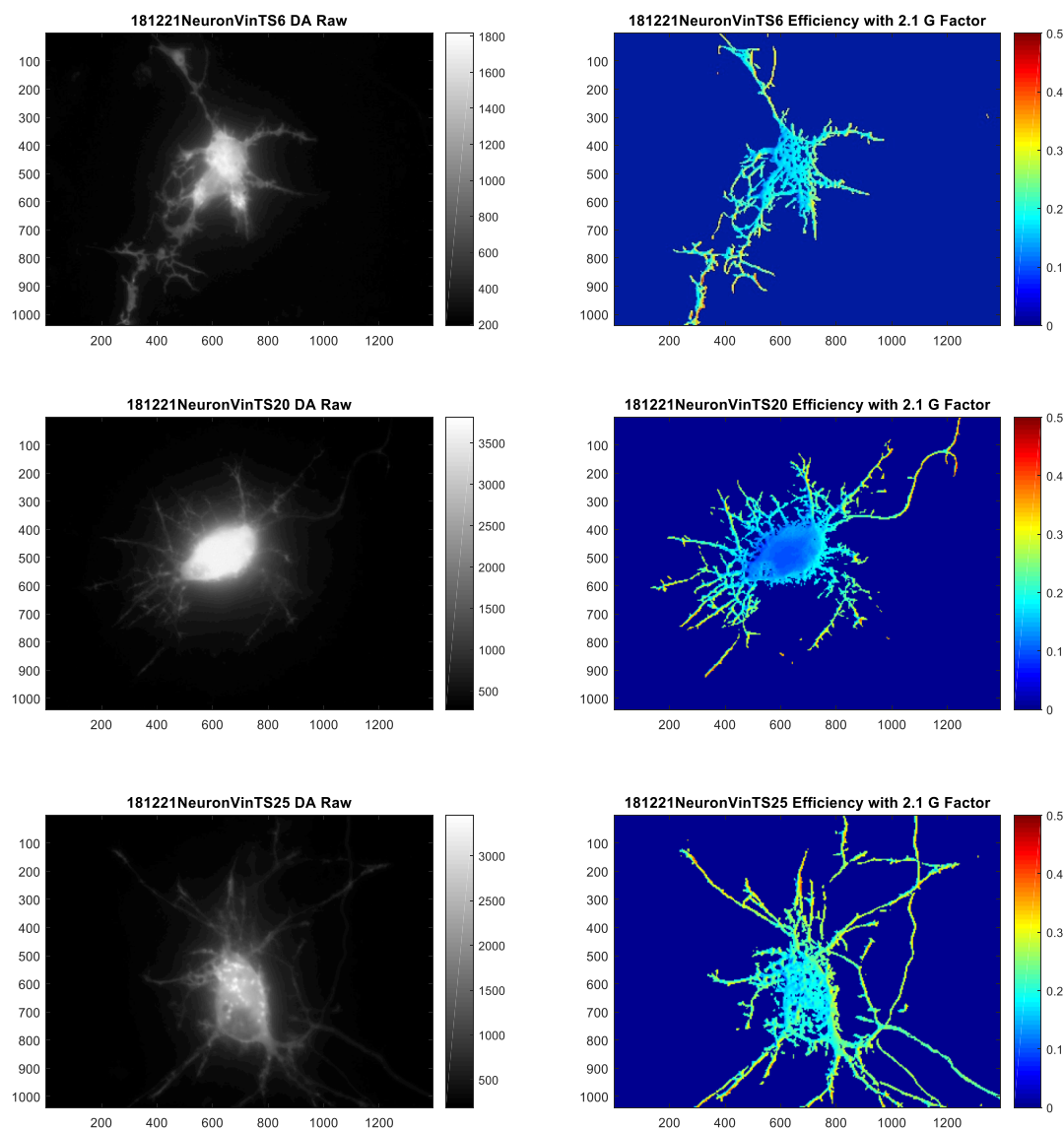
Figure 28: Processed VinTS Neurons showing E_{FRET} in different areas throughout the cell
(Field of View: 90 μm by 70 μm)
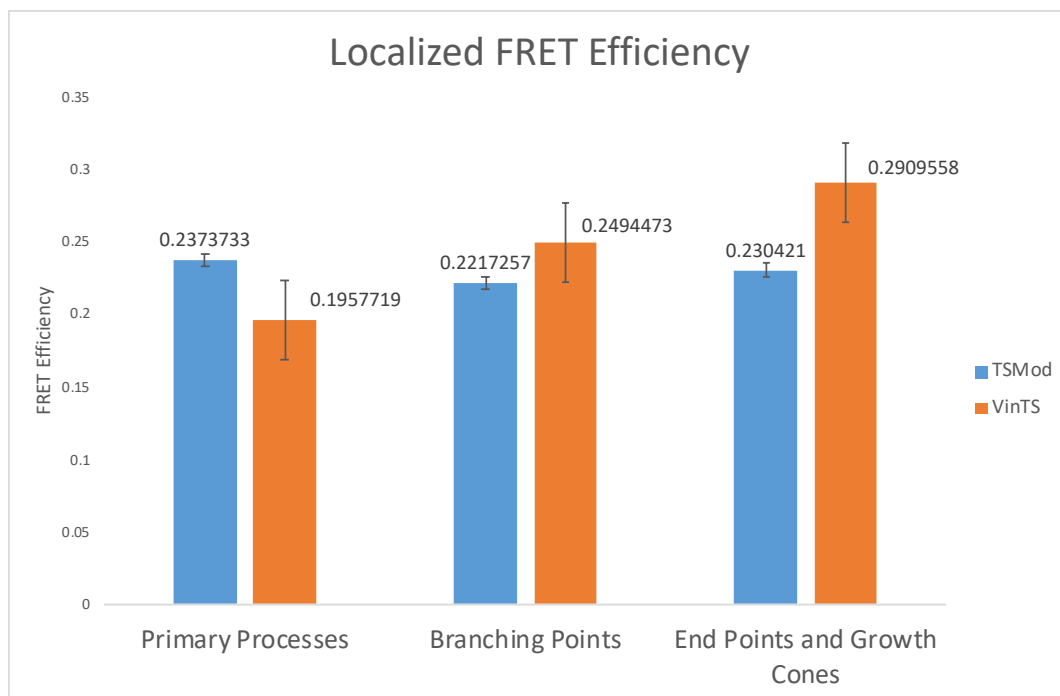
Figure 29: Average FRET Efficiency in different areas of TSMod and VinTS Neurons

	TSMod		
	Primary Processes	**Branching Points**	**End Points and Growth Cones**
	0.203	0.227	0.180
	0.224	0.196	0.221
	0.262	0.257	0.222
	0.242	0.234	0.245
	0.245	0.195	0.261
	0.237	0.203	0.263
	0.232	0.227	0.192
	0.244	0.197	0.232
	0.241	0.242	0.236
	0.244	0.239	0.251
Average	0.237	0.222	0.230
Standard Deviation	0.016	0.022	0.027

Table 11: Selected FRET Efficiency Values in different Areas of TSMod Neurons

	VinTS		
	Primary Processes	**Branching Points**	**End Points and Growth Cones**
	0.235	0.257	0.246
	0.160	0.268	0.255
	0.205	0.261	0.280
	0.197	0.271	0.302
	0.174	0.270	0.326
	0.181	0.237	0.301
	0.174	0.232	0.325
	0.223	0.254	0.317
	0.216	0.223	0.290
	0.193	0.222	0.268
Average	0.196	0.249	0.291
Standard Deviation	0.024	0.019	0.028

Table 12: Selected FRET Efficiency Values in different Areas of VinTS Neurons

An increase is seen in the E_{FRET} of the growth cones and end points between the TSMod and VinTS samples. This is most likely where most of the construct has moved to after transfection. The decrease in the E_{FRET} seen in the Primary Processes, appears to further indicate that there is a higher expression of the construct the end of the processes. It also appears to support the idea that there is more force at the Branching Points as well as The End Points and Growth Cones, which is in line with what is currently understood about neuronal growth.

3.4: Discussion of Results in Neurons

When the DD/AA values from the neuronal dataset were first analyzed and a wide range of the values was made evident, the issue of photobleaching was the first consideration. This caused an adjustment in the image acquisition procedure to minimize exposure to light that could photobleach the sample. In addition to the earlier reduction of power, a Neutral Density (ND) Filter was also added to further reduce the power of the incident light. A narrowing of the DD/AA range was noticed, but the collected data was

not as tightly packed as the iBMK and BAEC data. This has raised the issue of an issue specific to neurons.

The variability seen in the DD/AA values of the neuronal data is believed to be due to intermolecular construct interactions. This is when a large amount of FRET is generated between constructs, instead of within them. It has been previously shown that intermolecular interactions are negligible within Focal Adhesions.[25] Neurons, however, have not been tested as frequently, so intermolecular interactions cannot be ruled out. One of the biggest discoveries and conclusions that has been drawn is that areas of high signal, which were initially thought to be the target area for imaging, may not be the optimal locations to image. These areas are mainly cell bodies, where it is believed there is a higher density of constructs. Instead, the focus of imaging within the neuronal line has shifted to processes. This area has shown more promising results, with DD/AA values closer to what is expected. They are also more relevant to the future directions of the project, as neuronal growth cones are the next area of study.

The large range of variation of the DD/AA values obtained for the neurons made calibration very difficult. It required additional exclusion parameters to be developed to obtain a G Factor in line with the expected value of approximately 2.1. This involved manual exclusion of outlier points based on visual observation. Similar to how outliers were excluded in the iBMK and BAEC lines, points that were far removed from the central cloud of points were deemed outliers. All points with DD/AA values above 4 were excluded for both the TRAF and (GGSGGS)$_2$ datasets. In addition, for the (GGSGGS)$_2$ data, all points with a DD/AA value above 2.5 were excluded. This value was chosen as it maximizes the number of inclusion points, while retaining a G Factor

around 2.1. From earlier studies it is understood that the DD/AA values of the (GGSGGS)$_2$ datasets are never larger than half of the max TRAF DD/AA values. Some leeway given, and the range of inclusion was increased to allow for maximum data inclusion. This, however, did not correct for the anomaly of the (GGSGGS)$_2$ E$_{FRET}$ not being around the target value.

The expression of the constructs in the neurons was also an area for concern. This is mainly due to the cells themselves being harder to transfect that the other two tested lines. The overall observed transfection efficiency of the neuronal cultures was consistently less than 10%. This low transfectability not only limited the number of samples that were able to be obtained, but it also influenced each of the collected samples themselves. The variation of expression, possibly due to their unique cell shape, within the neurons themselves only further exasperated this issue. This was discussed earlier on as well, but the large DD/AA range observed within the neuronal samples may be due to the unequal expression and distribution of the constructs. This concern has caused a new Lentiviral Vector method to be investigated and implemented for future experimentation in neurons.

CHAPTER 4: CONCLUSIONS, DISCUSSION, AND FUTURE DIRECTIONS

While results were able to be obtained both within the iBMK and BAEC lines,

they were not without their challenges. One of the biggest was the proper correction of

the background. As discussed earlier, a histogram-based approach was utilized for

background correction. This method appears to work and properly correct for the

background in theory, but a new approach may be necessary. An area of future

investigation is the comparison of the current histogram-based method to a sample-based

method. This would entail the obtaining image sets from non-expressing areas of the

coverslip. This method may account for sample-to-sample variability, accounting for

possible inherent cellular variation that could affect the measured background.

The issue of photobleaching also affected many of the samples. Early data

collected indicated that samples were photobleaching, as signal was low, and the

measured power was very high. A reduction in the power of the excitation light was done

to correct for this. This was done through a reduction in the size of the aperture through

which the light passed. The reported iBMK and BAEC samples were collected after this

correction with the 63x objective. The issue appeared to be corrected for, but the issue

arose again after a bulb change in the Hg Arc Lamp. This change occurred right before

collection of data from the transfected neuronal culture samples. The issue remained

present during an additional trial with iBMK samples. The power levels were measured

with both objectives. Through the 63x objective, power values of 33mW with the mTFP1

filter and 2.55mW with the mVenus filter were measured. After closure with the 63x,

values of 10.8mW and 0.9mW were obtained, for the mTFP1 and mVenus filters

respectively. With the 40x objective, an open aperture value for the mTFP1 filter of

100mW and a closed aperture value of 15.2mW were measured. The 40x objective power values for the mVenus filter were 7.1mW and 1.2mW for the open and closed positions.

As discussed earlier in Section 3.4, a ND filter was added to the setup, and the power levels were remeasured through the 40x objective. For the mTFP1 filter, an open aperture value of 81.7mW and closed value of 13.5mW were recorded. Through the mVenus filter, values of 8.9mW and 1.47mW were observed. Measurements through both of the ND filters, with closed aperture positions, were taken as well. For the 0.1 ND Filter, values of 12mW and 1.24mW were observed for the mTFP1 and mVenus filters, respectively. Measurements taken with the 0.3 ND Filter and closed aperture gave a measurement of 9.1mW for the mTFP1 filter and 0.92mW for the mVenus filter. The current imaging methodology has been adjusted to image using either of the ND Filters with closed aperture to optimize power reduction.

One of the major differences between the iBMK and BAEC lines and Neurons is the cell shape. While iBMK and BAEC cells are composed of solely a cell body, neurons have processes which extend out from the cell body. These processes can cause a variation in the distribution and therefore expression of the construct. Most of the neuron data reported here is of solely the cell body, due to the fact that there appeared to be more expression there. The few images that were obtained of the neuronal processes appear to have E_{FRET} values which are more consistent with what was expected. This means that when imaging neurons, it is better to image the neuronal processes than the cell body, even if there is more signal in the cell body. This may be due to intermolecular interactions between expressed FRET constructs in the cell body, but this conclusion, however, will require further testing to validate. The thickness of the imaged areas,

especially when the area is out-of-focus, could also have an impact on the measured E_{FRET}. This arises from the possibility that the signal for each channel may be more difficult to register. The issue may not arise for the TRAF, (GGSGGS)$_2$, and TSMod constructs but may have an impact on the images obtained from samples transfected with VinTS.

Another area of concern is the difficulty in the removal of the nucleus from the final images. A simple thresholding method could be applied, but this could remove the edges of the Focal Adhesions within the iBMK and BAEC samples. This is important as clear edges of the Focal Adhesions are needed for proper assessment of the forces within them. When this thresholding method was attempted, in many cases, the removal of the nucleus was not possible without affecting the Focal Adhesions. In addition, the nucleus, which does not express the constructs, can influence the calculated F_c/AA and DD/AA values. This is due to the fact that the calculations are done on a pixel-by-pixel basis. A blanket thresholding could also affect the calculation of these values, due to the fact that an over thresholding could skew the calculated slopes.

A further improvement to the computational processing methodology is the implementation of a more precise segmentation algorithm for the Focal Adhesions. The "water" algorithm has been used in previous studies to isolate Focal Adhesions.[25, 27, 37] This algorithm was developed from "a modified 'lake' algorithm," which is able to isolate the Focal Adhesions by sorting pixel values and excluding areas smaller than a minimum area.[48] The mask approach described earlier can isolate the focal adhesions, but it works by using a disk to create a mask. This approach is limited by the size of the disk, whereas the "water" algorithm only requires a minimum area. The disk size may

need to vary between cells, so using a blanket value is not optimal. The "water" algorithm also has more flexibility to account for Focal Adhesions or expressive areas of a variety of sizes. The mask method is very sensitive to the disk size, so a varying disk size with that method would not work. The independence and variably of the "water" algorithm make it an area worth investigation and implementation.

In addition, integration of the "Binning" methodology into the iBMK and BAEC processing is currently in development. This method uses a square grouping of 4-by-4 pixels, similar to the neuronal method. This combined with the creation of the dilation mask could improve the isolation of the Focal Adhesions, as well as improve the measured signal of the constructs in the region of interest.

Another way to calculate the G Factor is through the use of the mode of all pixel values from all images. This may produce a more accurate and consistent G Factor. This is done through the creation of a heatmap of all pixel values for both of the control constructs, then calculation of the mode of each of the clouds created.[37] This method appears to inherently disregard outlier points both within and between samples, leading to a more precise and consistent G Factor. A lab-developed version of this methodology is currently being developed, but the isolation of each control construct's cloud required work. The current version has overcome this and is in the earlier stages of testing with the data present throughout this work. This new method has also caused a reevaluation of the background correction methodology and an investigation into further isolation of the region of interest, both described earlier. In addition, a method for E_{FRET} optimization has also been looked into. This method would involve the use of "bootstrapping" the mode of values to further optimize the calculation, improving E_{FRET} closer to the

expected value. [37] The integration of this practice is still under consideration, but it appears to be a valid method if sufficient data is not able to be obtained from a given available data set.

In all, the experiments described here provide a foundation for future studies. The imaging setup and methodology can successfully measure E_{FRET} that is within the expected range. It was also discovered that cell type may have an effect on the measured result. The neuron appears to be a viable test subject but may not be able to be used as a calibration cell type. The iBMK and BAEC lines produce comparable results, but certain exclusion parameters must be applied due to the nature of the calculation method. The image processing technique can also reliably produce interpretable E_{FRET} images, but the quantitative method for G Factor calculation may need to be improved. The insecurity and variability noticed in the implementation of the mathematical approach to G Factor calculation supports this idea.

The conclusions reached and presented here should be viewed as they are presented, rooted in a series of assumptions and created from a single method. There are a multitude of approaches to calculating E_{FRET} and the cell types in which they were determined could have an effect on their use. The neuron as a test subject is novel and work done in this area is rudimental. The work done here establishes a baseline for further study and optimization of E_{FRET} measurements in neurons, as well as demonstrates that cell type has an effect on measurement. Careful consideration must be done when deciding to test in a new cell type, as well as in the determination of what cell types will be tested. This consideration must play a key role in experimental planning and design, as a lack of consideration could derail a project plan. Overall, E_{FRET} and it uses as

a tool will allow for insight into cellular level mechanical forces, furthering

understanding into how cells operate within their microenvironment.

REFERENCES

[1]   E. A. Jares-Erijman and T. M. Jovin, "FRET imaging," *Nature biotechnology,* vol. 21, no. 11, p. 1387, 2003.

[2]   E. Betzig and J. K. J. S. Trautman, "Near-field optics: microscopy, spectroscopy, and surface modification beyond the diffraction limit," vol. 257, no. 5067, pp. 189-195, 1992.

[3]   B. Huang, M. Bates, and X. J. A. r. o. b. Zhuang, "Super-resolution fluorescence microscopy," vol. 78, pp. 993-1016, 2009.

[4]   R. M. Clegg, "The history of FRET," in *Reviews in Fluorescence 2006*: Springer, 2006, pp. 1-45.

[5]   B. T. Bajar, E. S. Wang, S. Zhang, M. Z. Lin, and J. Chu, "A guide to fluorescent protein FRET pairs," *Sensors,* vol. 16, no. 9, p. 1488, 2016.

[6]   J. R. Albani, *Structure and dynamics of macromolecules: absorption and fluorescence studies*. Elsevier, 2011.

[7]   Y. Sun, C. Rombola, V. Jyothikumar, and A. Periasamy, "Förster resonance energy transfer microscopy and spectroscopy for localizing protein–protein interactions in living cells," *Cytometry Part A,* vol. 83, no. 9, pp. 780-793, 2013.

[8]   H. Chen, H. L. Puhl 3rd, S. V. Koushik, S. S. Vogel, and S. R. Ikeda, "Measurement of FRET efficiency and ratio of donor to acceptor concentration in living cells," *Biophysical journal,* vol. 91, no. 5, pp. L39-L41, 2006.

[9]   R. B. Sekar and A. Periasamy, "Fluorescence resonance energy transfer (FRET) microscopy imaging of live cell protein localizations," *The Journal of cell biology,* vol. 160, no. 5, pp. 629-633, 2003.

[10]   S. M. Müller, H. Galliardt, J. Schneider, B. G. Barisas, and T. Seidel, "Quantification of Förster resonance energy transfer by monitoring sensitized emission in living plant cells," *Frontiers in plant science,* vol. 4, p. 413, 2013.

[11]   T. W. Gadella Jr, T. M. Jovin, and R. M. J. B. c. Clegg, "Fluorescence lifetime imaging microscopy (FLIM): spatial resolution of microstructures on the nanosecond time scale," vol. 48, no. 2, pp. 221-239, 1993.

[12]   H. Wallrabe and A. J. C. o. i. b. Periasamy, "Imaging protein molecules using FRET and FLIM microscopy," vol. 16, no. 1, pp. 19-27, 2005.

[13]   M. Peter *et al.*, "Multiphoton-FLIM quantification of the EGFP-mRFP1 FRET pair for localization of membrane receptor-kinase interactions," vol. 88, no. 2, pp. 1224-1237, 2005.

[14]   S. Padilla-Parra, N. Audugé, M. Tramier, and M. J. C. S. H. P. Coppey-Moisan, "Time-domain fluorescence lifetime imaging microscopy: a quantitative method to follow transient protein–protein interactions in living cells," vol. 2015, no. 6, p. pdb. top086249, 2015.

[15]   Y. Chen, J. D. Mills, and A. J. D. Periasamy, "Protein localization in living cells and tissues using FRET and FLIM," vol. 71, no. 9-10, pp. 528-541, 2003.

[16]   R. N. Day, C. F. Booker, and A. Periasamy, "Characterization of an improved donor fluorescent protein for Förster resonance energy transfer microscopy," *Journal of biomedical optics,* vol. 13, no. 3, p. 031203, 2008.

[17] H.-w. Ai, J. N. Henderson, S. J. Remington, and R. E. J. B. J. Campbell, "Directed evolution of a monomeric, bright and photostable version of Clavularia cyan fluorescent protein: structural characterization and applications in fluorescence imaging," vol. 400, no. 3, pp. 531-540, 2006.

[18] A. Rekas, J.-R. Alattia, T. Nagai, A. Miyawaki, and M. J. J. o. b. c. Ikura, "Crystal structure of venus, a yellow fluorescent protein with improved maturation and reduced environmental sensitivity," vol. 277, no. 52, pp. 50573-50578, 2002.

[19] T. Nagai, K. Ibata, E. S. Park, M. Kubota, K. Mikoshiba, and A. J. N. b. Miyawaki, "A variant of yellow fluorescent protein with fast and efficient maturation for cell-biological applications," vol. 20, no. 1, p. 87, 2002.

[20] P. Sarkar, S. V. Koushik, S. S. Vogel, I. Gryczynski, and Z. K. J. J. o. b. o. Gryczynski, "Photophysical properties of Cerulean and Venus fluorescent proteins," vol. 14, no. 3, p. 034047, 2009.

[21] K. Aoki, N. Komatsu, E. Hirata, Y. Kamioka, and M. Matsuda, "Stable expression of FRET biosensors: a new light in cancer research," *Cancer science,* vol. 103, no. 4, pp. 614-619, 2012.

[22] H.-G. Wang *et al.*, "Ca2+-induced apoptosis through calcineurin dephosphorylation of BAD," *Science,* vol. 284, no. 5412, pp. 339-343, 1999.

[23] X. Michalet *et al.*, "Quantum dots for live cells, in vivo imaging, and diagnostics," vol. 307, no. 5709, pp. 538-544, 2005.

[24] V. Venugopal, J. Chen, M. Barroso, and X. J. B. o. e. Intes, "Quantitative tomographic imaging of intermolecular FRET in small animals," vol. 3, no. 12, pp. 3161-3175, 2012.

[25] C. Grashoff *et al.*, "Measuring mechanical tension across vinculin reveals regulation of focal adhesion dynamics," *Nature,* vol. 466, no. 7303, p. 263, 2010.

[26] A. S. LaCroix, K. E. Rothenberg, M. E. Berginski, A. N. Urs, and B. D. Hoffman, "Construction, imaging, and analysis of FRET-based tension sensors in living cells," in *Methods in cell biology*, vol. 125: Elsevier, 2015, pp. 161-186.

[27] A. S. LaCroix, A. D. Lynch, M. E. Berginski, and B. D. Hoffman, "Tunable molecular tension sensors reveal extension-based control of vinculin loading," *Elife,* vol. 7, p. e33927, 2018.

[28] S. V. Koushik, H. Chen, C. Thaler, H. L. Puhl III, and S. S. Vogel, "Cerulean, Venus, and VenusY67C FRET reference standards," *Biophysical journal,* vol. 91, no. 12, pp. L99-L101, 2006.

[29] K. E. Rothenberg, S. S. Neibart, A. S. LaCroix, and B. D. Hoffman, "Controlling cell geometry affects the spatial distribution of load across vinculin," *Cellular and Molecular Bioengineering,* vol. 8, no. 3, pp. 364-382, 2015.

[30] K. E. Rothenberg, I. Puranam, and B. D. Hoffman, "Measurement of Force-Sensitive Protein Dynamics in Living Cells Using a Combination of Fluorescent Techniques," *JoVE (Journal of Visualized Experiments),* no. 141, p. e58619, 2018.

[31] I. Puranam, A. Urs, B. Kirk, K. Newell-Litwa, and B. Hoffman, "A Molecular Tension Sensor for N-Cadherin Reveals Distinct Forms of Mechanosensitive Adhesion Assembly in Adherens and Synaptic Junctions," *bioRxiv,* p. 552802, 2019.

[32]   M. J. Sullivan and G. C. Ulett, "Stable expression of modified green fluorescent protein in group B streptococci to enable visualization in experimental systems," *Appl. Environ. Microbiol.,* vol. 84, no. 18, pp. e01262-18, 2018.

[33]   C. S. H. L. Press. (2015). *Valap Sealant.*

[34]   B. L. Scott and A. D. Hoppe, "Optimizing fluorescent protein trios for 3-Way FRET imaging of protein interactions in living cells," *Scientific reports,* vol. 5, p. 10270, 2015.

[35]   H. Wallrabe, Y. Sun, X. Fang, A. Periasamy, and G. Bloom, "Three-Color FRET expands the ability to quantify the interactions of several proteins involved in actin filament nucleation," in *Multiphoton Microscopy in the Biomedical Sciences XII*, 2012, vol. 8226: International Society for Optics and Photonics, p. 82260J.

[36]   D. Shrestha, A. Jenei, P. Nagy, G. Vereb, and J. J. I. j. o. m. s. Szöllősi, "Understanding FRET as a research tool for cellular studies," vol. 16, no. 4, pp. 6718-6756, 2015.

[37]   E. M. Gates, A. S. LaCroix, K. E. Rothenberg, and B. D. Hoffman, "Improving Quality, Reproducibility, and Usability of FRET-Based Tension Sensors," *Cytometry Part A,* vol. 95, no. 2, pp. 201-213, 2019.

[38]   J. Iwasa and W. F. Marshall, *Karp's Cell and Molecular Biology: Concepts and Experiments*. John Wiley & Sons, 2016.

[39]   R. Mathew, K. Degenhardt, L. Haramaty, C. M. Karp, and E. White, "Chapter 5 Immortalized Mouse Epithelial Cell Models to Study the Role of Apoptosis in Cancer," Elsevier, 2008, pp. 77-106.

[40]   A. S. LaCroix and B. Hoffman, "FRET data and calculation of FRET efficiency from sensitized emission," N. N. Boustany, Ed., ed, 2018.

[41]   K. Schregel *et al.*, "Demyelination reduces brain parenchymal stiffness quantified in vivo by magnetic resonance elastography," *Proceedings of the National Academy of Sciences,* vol. 109, no. 17, pp. 6650-6655, 2012.

[42]   D. M. Geddes-Klein, K. B. Schiffman, and D. F. Meaney, "Mechanisms and consequences of neuronal stretch injury in vitro differ with the model of trauma," *Journal of neurotrauma,* vol. 23, no. 2, pp. 193-204, 2006.

[43]   D. M. Suter and P. Forscher, "Substrate–cytoskeletal coupling as a mechanism for the regulation of growth cone motility and guidance," *Journal of neurobiology,* vol. 44, no. 2, pp. 97-113, 2000.

[44]   A. M. Sydor, A. L. Su, F.-S. Wang, A. Xu, and D. G. Jay, "Talin and vinculin play distinct roles in filopodial motility in the neuronal growth cone," *The Journal of cell biology,* vol. 134, no. 5, pp. 1197-1207, 1996.

[45]   S. C. Noctor, A. C. Flint, T. A. Weissman, R. S. Dammerman, and A. R. Kriegstein, "Neurons derived from radial glial cells establish radial units in neocortex," *Nature,* vol. 409, no. 6821, p. 714, 2001.

[46]   R. Annunziata and E. Trucco, "Accelerating convolutional sparse coding for curvilinear structures segmentation by refining SCIRD-TS filter banks," *IEEE transactions on medical imaging,* vol. 35, no. 11, pp. 2381-2392, 2016.

[47]   R. Annunziata, A. Kheirkhah, P. Hamrah, and E. Trucco, "Scale and curvature invariant ridge detector for tortuous and fragmented structures," Springer, pp. 588-595.

[48]   E. Zamir, B.-Z. Katz, S.-i. Aota, K. M. Yamada, B. Geiger, and Z. J. J. o. c. s. Kam, "Molecular diversity of cell-matrix adhesions," vol. 112, no. 11, pp. 1655-1669, 1999.